Rare Met. (2021) 40(10):2657–2689
https://doi.org/10.1007/s12598-020-01694-w

RARE METALS

REVIEW

Recent advances in carbonized non-noble metal–organic frameworks for electrochemical catalyst of oxygen reduction reaction

Chan Li, Dao-Hui Zhao, Hua-Li Long*, Ming Li*

Received: 6 July 2020 / Revised: 14 October 2020 / Accepted: 23 December 2020 / Published online: 26 April 2021

Abstract The non-noble metal oxygen reduction reaction (ORR) catalysts prepared by carbonization of metal–organic framework (MOF) have attracted more and more attentions in the fields of fuel cells and metal-air batteries due to their unique intrinsic advantages such as high catalytic activity, low price, simple synthesis and good adaptability. Different from the study of traditional high active noble metal catalysts, this review systematically summarizes recent developments on non-noble metal (Fe, Co, Cu, Ni, Mn and Mo) ORR catalysts prepared by various MOFs carbonization in different metal centers. The effects of synthesis strategies and pyrolysis conditions on the catalyst properties are discussed. Meanwhile, the key parameters of catalytic performances (including active sites, dispersed state and specific surface area) are discussed and the prospect is presented. It is expected that this review will provide effective guidance for future studies on carbonized non-noble MOFs for ORR electrochemical catalyst.

Keywords Non-noble metal; MOF; Pyrolysis; Catalyst; ORR

1 Introduction

Metal–organic framework (MOF) was first reported in 1995 [1, 2], which is made of various organic ligands and metal ions (Zn^{2+}, Cr^{3+}, Cu^{2+}, Co^{2+}, etc.), with a series of advantages such as adjustable porous structure and porosity, low crystal density, ultrahigh specific surface area and highly ordered pore structure. With these functions, MOF can be used for gas storage, nano-separation, biomedicine, proton conduction, nano-reactor, energy conversion and so on [3–8]. Many new MOFs with unique characteristics, such as the Materials of Institute Lavoisier (MIL) with large specific surface area (5900 $m^2 \cdot g^{-1}$ for MIL-101) and the topologically structured zeolite-like MOF (ZIF), are designed by different metal ions and organic ligands with different sizes [9, 10]. With the continuous development of MOFs, they have become research hotspots in various fields. However, in the research process of MOFs, there are still some inevitable shortcomings, such as low stability in acid and water, and low conductivity, especially the latter greatly restricts their application in the field of electrochemistry [11, 12]. In order to overcome these shortcomings, researchers have developed stable and conductive MOF catalysts through structural design or composite materials with conductive substrates, but their effects are far inferior to other metal-based catalysts [13, 14]. However, due to the large specific surface area and heteroatom doping, MOFs are found to be excellent precursors of carbon-based catalysts [15].

Oxygen reduction reaction (ORR) is one of the most important cathode reactions in fuel cells and metal-air batteries [16, 17]. Usually, these are divided into 2-electron and 4-electron reaction processes (Fig. 1 [18]). Generally, the advantages of 4-electron process include the avoidance

---

Chan Li and Dao-Hui Zhao have contributed equally to this work.

C. Li, D.-H. Zhao, H.-L. Long*, M. Li*
Hubei Collaborative Innovation Center for Advanced Organic Chemical Materials, Ministry-of-Education Key Laboratory for the Synthesis and Application of Organic Functional Molecules, Hubei Key Laboratory of Polymer Materials, College of Chemistry and Chemical Engineering, Hubei University, Wuhan 430062, China
e-mail: lililong_007@163.com

M. Li
e-mail: liming@hubu.edu.cn

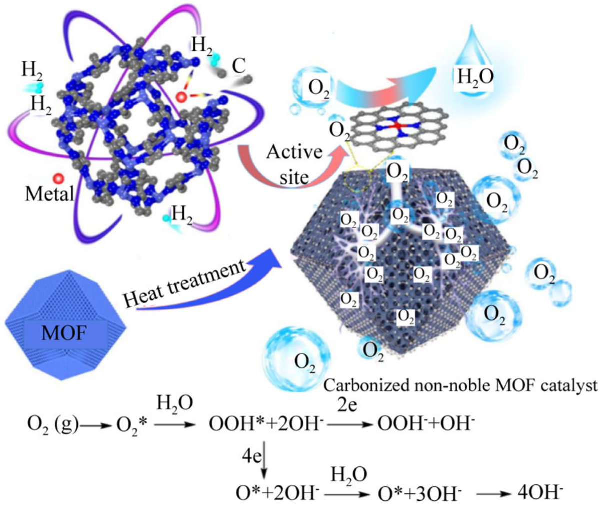

Fig. 1 Schematic diagram of ORR process by MOF-based catalyst. Reproduced with permission from Ref. [18]. Copyright 2019 Elsevier Ltd.

of damage to the catalyst by H_2O_2 and a higher theoretical cathode voltage. The ideal ORR requires a small overpotential, which helps to improve the battery's output voltage and energy efficiency. Therefore, the design of the 4-electron process ORR catalyst with excellent performance has received extensive attention. Currently, the most used and commercially available ORR catalyst is the Pt/C catalyst. A small amount of Pt/C catalyst can achieve satisfactory ORR catalytic performance. However, the Pt/C catalyst is limited by high price, low catalytic stability and cycle efficiency, which indicates that it is urgent to develop low-cost, exciting activity, high stability and green catalysts to replace Pt/C. Compared with noble metal catalysts, non-noble metal catalysts, such as transition metal–nitrogen–carbon (M–N–C, M = Fe, Co, Ni, Cu, etc.) catalysts or transition metal oxide catalysts, have natural electrocatalysis and price advantages [19–21]. Although there are many ways to prepare non-noble metal catalysts, the preparation by MOF carbonization has the following advantages: (1) The catalyst performance can be optimized by designing the precursor structure of MOF and controlling pyrolysis conditions; (2) The metal center of MOF and other doped heteroatoms can provide the catalytic active centers; (3) During the pyrolysis of the MOF precursor, the graphene carbon structure or carbon nanotube (CNT) structure can be formed, which helps to improve electrical conductivity. Therefore, the preparation of non-noble metal catalysts by MOF carbonization is an attractive synthetic route [22].

Currently, there are several important parameters to evaluate the ORR performance of catalysts: (1) The onset potential (E_{onset}) is the voltage at which the ORR occurs and is usually obtained at a current density of 1 mA·cm^{-2}. The higher the onset potential, the smaller the overpotential and the higher energy conversion efficiency. (2) The half-wave potential ($E_{1/2}$) is the electrode potential when the current density of the reaction is equal to half of the limiting diffusion current density. It can qualitatively analyze the catalyst because the value depends on the inherent nature of the catalyst. (3) The Tafel slope reflects the kinetic rate of the ORR process. The smaller the Tafel slope, the faster the ORR kinetics of the catalyst. (4) As mentioned above, it is extremely important for ORR to reveal whether the reaction adopts a 2-electron or 4-electron process. There are two specific calculation methods: one is to calculate the electron transfer number through the Koutecky–Levich equation (Eq. (1)); another method is to monitor the H_2O_2 yield (Eq. (2)) in the catalytic process by rotating ring-disk electrode (RRDE) and calculate the electron transfer number (Eq. (3)). (5) The cyclic stability is mainly used to describe the catalyst durability. In addition, the synthesis method of the catalyst ink, the amount and thickness of electrode coatings, the electrolyte composition and the rate of ORR linear sweep voltammetry (LSV) will also affect the performance of the catalyst [23–25].

$$\frac{1}{J}=\frac{1}{J_{\mathrm{L}}}+\frac{1}{J_{\mathrm{K}}}=\frac{1}{J_{\mathrm{K}}}+\frac{1}{0.62nFC_0(D_0)^{2/3}\upsilon^{-1/6}\omega^{1/2}} \tag{1}$$

where J, J_{L} and J_{K} are the measured current density, diffusion limiting current density and kinetic current density, respectively. n is the number of electrons transferred, F is the Faraday constant, C_0 is the concentration of O_2 in solution, D_0 is the diffusion coefficient of O_2, υ is the kinetic viscosity of the solution, and ω is the rotation speed of the electrode.

$$w=200\frac{I_{\mathrm{R}}/N}{I_{\mathrm{D}}+I_{\mathrm{R}}/N} \tag{2}$$

$$n=4\frac{I_{\mathrm{D}}/N}{I_{\mathrm{D}}+I_{\mathrm{R}}/N} \tag{3}$$

where w refers to the yield of H_2O_2, I_{D} and I_{R} are disk current and ring current, respectively, and N refers to the collection efficiency of the ring.

Many reviews and comments of MOF-based catalysts have been published in recent years [15, 26], but most of them are too broad and do not focus on the synthesis and performance of non-noble metal-based catalysts prepared by MOF carbonization. In this paper, the preparation of ORR catalyst by MOF carbonization is reviewed. The relationship between the preparation method and the catalyst performance is also discussed. According to the classification of different metal centers, the main content is divided into two parts: single-component metal carbon catalysts represented by Fe, Co, etc., and some multi-metal carbon catalysts. This review may benefit the future development of MOF-based non-noble metal ORR catalysts with high performance.

2 MOF-based Fe–N–C catalyst

2.1 Introduction of MOF-based Fe–N–C catalyst

The Fe–N–C catalyst is an amazing ORR cathode catalyst with the advantages of low cost, high activity and good stability. Many studies have shown that the activity of Fe–N–C catalyst mainly comes from the Fe–N_x sites, but for different Fe–N–C catalysts, the x value is different. Some studies have revealed that Fe–N_4 structure is the most active component at the Fe–N_x site, while Fe–N_2 contributes less [27, 28]. Lai et al. [29] prepared the Fe–N–C catalysts by carbonizing MOF-derived precursor to study the activity of Fe–N_x sites (including FeN_5, FeN_4 and FeN_2). According to the density functional theory (DFT) calculation, the energy barrier of N–Fe–N_4 (0.67 eV) in ORR was lower than that of Fe–N_4 (0.75 eV) and Fe–N_2 (1.99 eV). The adsorption energy of N–Fe–N_4 for OH was 2.88 eV, which was close to Pt (111) (2.23 eV), but lower than that of Fe–N_4 (3.07 eV) and Fe–N_2 (4.38 eV). Therefore, N–Fe–N_4 is more likely to convert oxygen into water. In fact, it is difficult to directly prepare N–Fe–N_4 catalyst with high activity, most of which are mixtures of different Fe–N_x structures. In addition, in the pyrolysis of Fe-based MOF, excess iron will combine with adjacent carbon to form FeC_3 particles, which also contributes to the ORR process [30].

The preparation of MOF-based Fe–N–C catalyst can be divided into three strategies: (1) Direct pyrolysis of Fe-MOFs with the greatest advantage of being very simple; (2) Pyrolysis of MOFs with additional iron sources, which has the advantage of various MOF carriers and cheap iron sources; (3) Pyrolysis of heteroatom-doped MOFs, which can enhance the catalytic activity through heteroatoms such as N and S. For all preparation methods, the synthesis and selection of MOF precursors have a significant effect on the catalyst's performance.

2.2 Preparation of Fe–N–C catalyst by direct carbonization of Fe-MOFs

One-step pyrolysis of Fe-MOFs to prepare Fe–N–C catalyst is the simplest and most effective method, but the key is the synthesis of Fe-MOF precursors. Fe-MOF is mainly synthesized through the coordination of Fe ions and organic ligands. Therefore, the coordination number of Fe ions and the molecular structure of organic ligands play a key role in the micro-morphology and stability of Fe-MOF. For example, Li et al. [31] employed 4,5-dicyanoimidazole (DCI) and iron acetate as raw materials to synthesize an organic DCI-Fe-MOF sheet by one-pot method, which was pyrolyzed in a N_2 atmosphere at 700 °C for 2 h to give a carbonized catalyst Fe-DCI-700 (Table 1 [18, 31–43]). The design of MOF at the molecular level ensured the uniform distribution of active elements N, C and Fe in the MOF precursor, thus ensuring abundant and well-distributed high active sites in Fe-DCI-700. The carbon shell encased the iron carbide on the N-doped carbon shell structure was beneficial to ORR. The catalyst contained 61.5 wt% Fe, 7.6 at% N, Brunauer–Emmett–Teller (BET) specific surface area of 249 $m^2 \cdot g^{-1}$ and the Raman peak intensity ratio of D band and G band (I_D/I_G) was 1.2. The higher I_D/I_G value, the more carbon defects; while the lower the I_D/I_G value, the higher the degree of graphite [44]. Under the catalyst loads of 0.1 $mg \cdot cm^{-2}$ and in 0.1 $mol \cdot L^{-1}$ KOH (aq.), Fe-DCI-700 exhibited a half-wave potential of $-$ 0.152 V vs. Ag/AgCl, which was 17 mV higher than that of commercial Pt/C catalyst. The measured electron transfer number of Fe-DCI-700 was 3.67, manifesting that the ORR process mainly followed the 4-electron mechanism (Table 2 [18, 31–43]). The result was mainly due to the graphitized shells, the high content of pyridine and pyrrole N (7.67%), and the lamellar porous structure with high-surface area formed by the MOF precursor, which greatly facilitated the transport of the electrolyte and provided rich and accessible active sites.

Besides, the Fe-MOF precursor can be prepared by post-modification of hydrogen-bonded supramolecules. For instance, Zhou et al. [32] first synthesized BA-TAP by hydrogen bond between barbituric acid (BA) and 2,4,6-triaminopyrimidine (TAP), whose N atoms were further coordinated with $FeCl_3$ to obtain BA-TAP-Fe. After pyrolysis in N_2 atmosphere at 800 °C for 1 h, the final BA-TAP-Fe-800 catalyst was synthesized. BA-TAP-Fe-800 formed a dense crystal structure through hydrogen bonds, which avoided collapse in the pyrolysis process. The multiphase iron was anchored to the multistage N-doped graphitic carbon. The catalyst had a porous structure (BET: 232 $m^2 \cdot g^{-1}$) and a high graphitization degree (I_D/I_G: 0.85). It also showed an onset potential of 1.02 V (vs. RHE), which was higher than that of Pt/C catalyst (0.95 V (vs. RHE)). Moreover, it possessed good ORR performance with half-wave potential of 0.85 V (vs. RHE), Tafel slope of $-$ 66 $mV \cdot dec^{-1}$, and electron transfer number of 3.9. The reaction of organic iron complexes with evaporable metal salts (such as Zn (907 °C)) is another method to prepare Fe-MOF. During pyrolysis, vaporized metals will create more pores in the catalyst. For example, Song et al. [33] used $K_3Fe(CN)_6$ and $ZnCl_2 \cdot 6H_2O$ to synthesize $Zn_3[Fe(CN)_6]_2 \cdot xH_2O$ (ZnPBA) as precursor. During the pyrolysis of ZnPBA in N_2 atmosphere at 800 °C, Zn would

Table 1 Summary of synthesis of MOF-based Fe–N–C catalyst

Sample	Active site	MOF			Lord	Pyrolysis precursor	Pyrolysis conditions	Refs.
		Type	Central ion	Ligand				
DCI-Fe-700	Fe–N_x, Fe_3C	DCI-Fe	Iron acetate	4, 5-dicyanoimidazole (DCI)	–	DCI-Fe	700 °C (5 °C·min^{-1}, N_2, 2 h)	[31]
BA-TAP-Fe-800	Fe–N_x, Fe_3C	BA-TAP-Fe	$FeCl_3$	Barbituric acid (BA), 2, 4,6-triaminopyrimidine (TAP)	–	BA-TAP-Fe	800 °C (5 °C·min^{-1}, N_2, 1 h)	[32]
Fe/Fe_3-C@N–C-1	Fe–N_x, Fe_3C	ZnPBA	$ZnCl_2$	$K_3Fe(CN)_6$	–	ZnPBA	800 °C (5 °C·min^{-1}, N_2, 1 h)	[33]
Fe–N–C	Fe–N_x	ZIF	$Zn(NO_3)_2$	4,5-dicyanoimidazole	$Fe(acac)_2$	Fe/Zn-dicyanoimidazolate	900 °C (5 °C·min^{-1}, N_2, 3 h)	[34]
Fe–N–C-3	Fe–N_x	ZIF-8	$Zn(NO_3)_2$	2-methylimidazole	$Fe(acac)_3$	Fe@ZIF-8	950 °C (5 °C·min^{-1}, H_2/Ar = 1/9, 1 h)	[18]
C-Fe-ZIF-1.44-950	Fe–N_x	ZIF-8	$Zn(NO_3)_2$	2-methylimidazole	Ferrocene	ZIF-8, Ferrocene	150 °C (5 °C·min^{-1}, Ar, 2 h), 950 °C (3 h)	[35]
Fe@NMC-1	Fe–N_x	ZIF-8	$Zn(NO_3)_2$	2-methylimidazole	$Fe(acac)_3$, melamine	Fe-ZIF-8	900 °C (3 °C·min^{-1}, Ar, 3 h)	[36]
6%Fe–N–S CNN	Fe–N_x	ZIF-8	$Zn(NO_3)_2$	2-methylimidazole	$FeSO_4$, hydrazine hydrate	Fe-ZIF-8	900 °C (Ar, 3 h)	[37]
Fe–N_2-800	Fe–N_x Fe/Fe_3C	MIL-101-Fe	$Fe(NO_3)_3$	1,3,5-benzenetricarboxylic acid (H3BTC)	Hexamethylenetetramine (HMT)	HMT/MIL-100-Fe	800 °C (5 °C·min^{-1}, N_2, 5 h)	[38]
NC@Fe_3O_4-900-1.5	Fe–N N@Fe_3-O_4	MIL-101-Fe	$FeCl_3$	Terephthalic acid (H2BDC)	Polyaniline (PANI)	PANI-coated MIL-101-Fe	900 °C (N_2, 2 h)	[39]
$F_{0.2}N_{0.2}M_{0.2}$-900	Fe–N Fe/Fe_3C	MIL-53	$Fe(NO_3)_3$	2-aminoterephthalate (H2ATA)	$(NH_4)_2S_2O_8$, melamine	MIL-53, $(NH_4)_2S_2O_8$, melamine	240 °C (2 °C·min^{-1}, N_2, 2 h), 900 °C (2 °C·min^{-1}, N_2, 1 h)	[40]
HCSC-IV	Fe–N	MIL-88	$Fe(NO_3)_3$	2-aminoterephthalate	Polyacrylonitrile (PAN), $(NH_4)_2S_2O_8$,	u-HCSC-IV	240° C (2 °C·min^{-1}, N_2, 2 h), 800 °C (2 °C·min^{-1}, N_2, 1 h)	[41]
Fe_2N@NPC-500	Fe_2N	HKUST-1	$Cu(NO_3)_2$	1,3,5-benzenetricarboxlic	$FeCl_3$, FePc	Fe_2N@NPC	500 °C (NH_3, 3 h)	[42]
Fe/N/S-PC	Fe–N_x	UIO-66-NH_2	$ZrCl_4$	2-aminoterephthalic acid (NH_2-BDC)	NH_4SCN, $FeCl_3$	Fe/N/S@UIO-66-NH_2	800 °C (5 °C·min^{-1}, Ar, 1 h), 900 °C (5 °C·min^{-1}, Ar, 1 h)	[43]

Table 2 Summary of ORR electrocatalytic activities of MOF-based Fe–N–C catalyst

Catalyst	Fe content	Hetero⁻ atom content	I_D/I_G	S_{BET}/ ($m^2 \cdot g^{-1}$)	Catalyst loading/ ($m^2 \cdot g^{-1}$)	Electrolyte (0.1 $mol \cdot L^{-1}$)	E_{onset}/V (vs. RHE)	$E_{1/2}$/V (vs. RHE)	Tafel slope/ ($mV \cdot dec^{-1}$)	n	H_2O_2 yield/ %	Refs.
DCI-Fe-700	61.50 wt%	7.6 at% N	1.200	249.00	0.100	KOH	–	− 0.152 (vs. Ag/AgCl)	–	3.67	–	[31]
BA-TAP-Fe-800	–	–	0.850	232.00	0.283	KOH	1.020	0.850	− 66.0	~ 3.90	~ 5.00	[32]
Fe/Fe_3-C@N-C-1	71.10 wt%	1.61 wt% N	–	182.50	0.480	KOH	0.936	0.804	–	4.08–4.15	3.50	[33]
Fe–N–C	–	–	0.830	407.00	0.450	KOH	0.997	0.910	–	3.95–3.99	2.00	[34]
						$HClO_4$	0.927	0.817	111.0	3.98	3.00	
Fe–N–C-3	–	–	0.886	1388.00	0.600	$HClO_4$	0.910	0.805	63.0	–	1.00	[18]
C-Fe-ZIF-1.44-950	1.00 wt%	5.51 at% N	–	1255.00	0.500	KOH	–	0.864	–	3.98	4.00	[35]
						$HClO_4$	–	0.780	–	3.97	2.00	
Fe@NMC-1	0.93 at%	11.82 at% N	1.040	793.30	0.200	KOH	1.010	0.880	54.0	3.90–3.99	0.37–7.58	[36]
						$HClO_4$	–	0.780	61.0	3.86–3.91	4.91–7.53	
6%Fe–N–S CNN	1.60 at%	9.65 at% N	–	974.00	–	KOH	–	0.910	–	~ 4.00	2.00	[37]
						H_2SO_4 (0.5 $mol \cdot L^{-1}$)	–	0.780	–	~ 4.00	1.00	
Fe–N_2-800	3.81 at%	4.02 at% N	0.882	138.00	0.500	KOH	− 0.077 (vs. SCE)	− 0.250 (vs. SCE)	85.0	3.76–3.91	9.20–16.80	[38]
NC@Fe_3O_4-900-1.5	–	–	–	698.52	0.663	KOH	0.058 (vs. Hg/HgO)	–	–	3.66 ~ 3.81	–	[39]
$F_{0.2}N_{0.2}M_{0.2}$-900	0.62 at%	3.25 at% N, 0.82 at% S	0.930	90.00	1.000	KOH	0.970	0.873	99.8	3.92–3.99	0.30–3.52	[40]
HCSC-IV	–	–	0.930	90.50	–	KOH	0.918	0.794	124.6	3.98	10.01	[41]
Fe_2N@NPC-500	0.11 wt%	1.89 wt% N	–	381.40	0.100	KOH	− 0.038 (vs. Ag/AgCl)	− 0.175 (vs. Ag/AgCl)	–	3.70–3.96	10.00	[42]
Fe/N/S-PC	0.31 at%	4.93 at% N, 1.49 at% S	1.190	1589.00	0.500	KOH	0.970	0.870	–	3.93–4.00	–	[43]
						$HClO_4$	0.890	0.785	–	3.50–3.65	–	

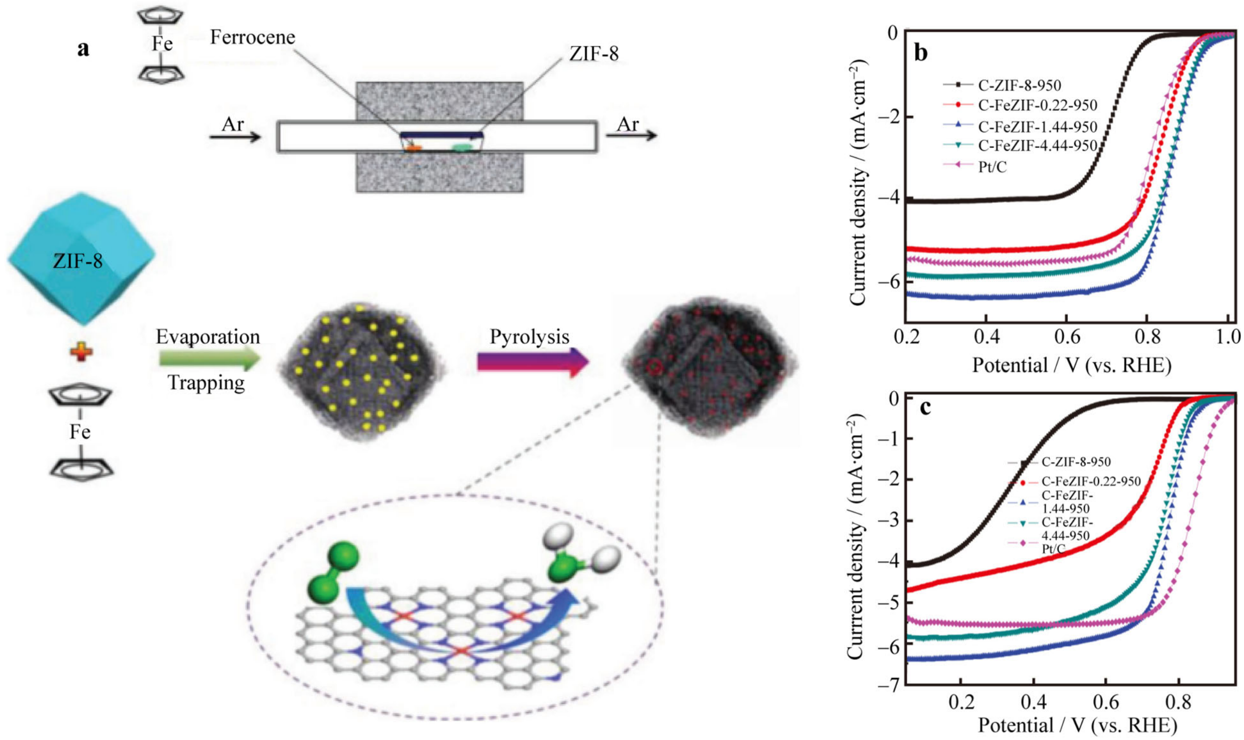

Fig. 2 **a** Schematic illustration of preparation of sample; LSV curves of sample in O_2-saturated **b** 0.1 mol·L^{-1} KOH and **c** 0.1 mol·L^{-1} $HClO_4$. Reproduced with permission from Ref. [35]. Copyright 2019 Wiley–VCH

evaporate to form pores and prevented Fe from agglomerating. With the increase of annealing time, the degree of graphitization also increased. At the same time, during the ZnPBA conversion, the cyano group (CN) was decomposed, releasing a large amount of carbon nitride gases, which could be captured by iron particles to catalyze the growth of CNTs. When the heating time was 1 h, the product (Fe/Fe_3C-C@N-C-1) had the maximum surface area of 182.5 m^2·g^{-1}, and contained 71.17 wt% iron and 1.61 wt% nitrogen, which was beneficial to the formation of Fe–N_x active sites and the improvement of ORR activity. The catalyst exhibited an onset potential of 0.936 V (vs. RHE), a half-wave potential of 0.804 V (vs. RHE), which was close to that of Pt/C (E_{onset} = 0.975 V (vs. RHE), $E_{1/2}$ = 0.820 V (vs. RHE)). After 1000 cycles, it was found that the half-wave potential of Fe/Fe_3C-C@N-C-1 catalyst had only a negative shift of 15 mV, which was smaller than that of the Pt/C catalyst (20 mV), indicating that its ORR catalytic effect was highly efficient and stable.

2.3 Preparation of Fe–N–C catalyst by carbonization of Fe-loaded MOFs

Although there are many types of MOFs, only MOFs with stable structure and N coordination site are suitable for direct Fe loading, and Fe–N–C catalysts with Fe–N_x active site can be prepared. As a subclass of MOF, ZIF is a zeolite-like porous crystalline material, usually consisting of Zn or Co and imidazole ligands. As for ZIF-8, it is a framework structure constructed by $Zn(NO_3)_2$·$6H_2O$ and 2-methylimidazole, which is regarded as an excellent carrier with rich N content and large specific surface area [45]. Shah et al. [34] mixed $Zn(NO_3)_2$·$6H_2O$, $Fe(acac)_2$ and 4,5-dicyanoimidazole in one pot to prepare Fe/Zn-dicyanoimidazolate. A series of Fe/Zn-dicyanoimidazolate frameworks with different contents were obtained through different molar ratios of Fe^{2+}/Zn^{2+}. After pyrolysis, highly active Fe–N_x and Fe_3C ORR sites were formed. By removing Fe_3C and Fe sites using acid etching, the performance of the catalyst was improved. The Fe–N–C catalyst showed excellent ORR performance in acidic and alkaline solutions. In 0.1 mol·L^{-1} KOH (aq.), it exhibited an onset potential of 0.997 V (vs. RHE), a half-wave potential of 0.91 V (vs. RHE) and 4-electron mechanism. Similarly, in 0.1 mol·L^{-1} $HClO_4$ (aq.), it had an onset potential of 0.927 V (vs. RHE), and a half-wave potential of 0.817 V (vs. RHE). Furthermore, the Fe–N–C catalyst displayed good stability in acidic and alkaline electrolytes, proving the excellent ORR catalyst. These results indicated that the coordination between iron ion and cyano group was the key to the synthesis of Fe–N_4 site, and Fe–N_x was more active for ORR than Fe_3C and Fe nanoparticles.

In addition, there are two forms of iron-loaded ZIF-8, namely in situ loading during the synthesis of ZIF-8 and

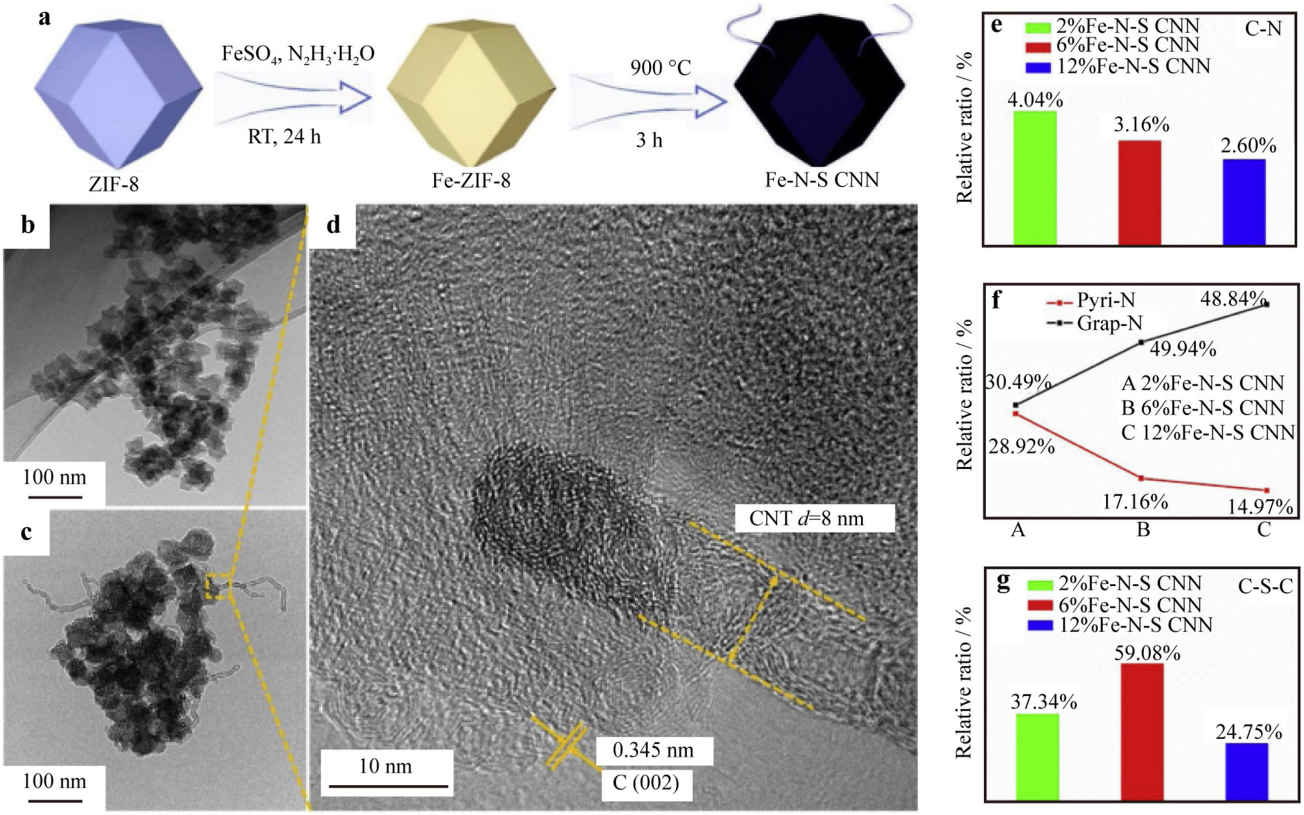

Fig. 3 **a** Schematic illustration of synthetic process for Fe–N–S CNN; **b** TEM image of CN; **c** TEM image; **d** HRTEM image of 6%Fe–N–S CNN; **e** C–N content; **f** pyridinic-N and graphitic-N; **g** C–S–C content in pyrolysis samples of different catalysts from XPS results. Reproduced with permission from Ref. [37]. Copyright 2019 Elsevier B.V.

loading by ZIF-8 to adsorb iron ions. Gao et al. [18] mixed Zn^{2+}, $Fe(acac)_3$ and 2-methylimidazole to prepare the Fe-loading Fe@ZIF-8. By controlling the ratio of H_2/Ar concentration in the pyrolysis atmosphere, it was found that when the H_2 content increased from 0% to 10%, the surface roughness of the pyrolysis product Fe–N–C was gradually enhanced, and the pore size enlarged from 1.23 to 2.36 nm. The specific surface area also increased from 961 to 1388 $m^{-2}·g^{-1}$. In order to improve ORR performance, it is very important to regulate the pore structure and active site density of Fe–N–C catalyst. As for the correlation mechanism between the density of the active site and H_2 concentration, hydrogen etching mainly etched unstable C, thus increasing the edge N and adjusting the pore structure. The edge N was then anchored to free iron atoms to form the Fe–N_x active sites. Meanwhile, the hydrogen etched the blocked carbon fragments to enlarge the pore size, leading to the formation of micro/mesopore structures. When H_2 concentration continued to increase, a large number of metal Fe particles that were inactive to ORR were formed, and the proportion of micropores was greatly reduced, resulting in a decrease in specific surface area. Therefore, when the H_2/Ar ratio was 1/9, Fe–N–C-3 catalyst had the best specific surface area (1388 $m^2·g^{-1}$), high graphitization degree (I_D/I_G: 0.886), and high ORR activity. It also had an onset potential of 0.91 V (vs. RHE), a half-wave potential of 0.805 V (vs. RHE), and ultralow H_2O_2 yield (1%). Moreover, one-pot preparation of iron-loaded MOF can achieve the purpose of in situ doping, and iron ions can be well dispersed [46]. For example, Deng et al. [35] took advantage of the easy sublimation of ferrocene (100 °C) to combine iron with ZIF-8 through gas adsorption (Fig. 2 [35]). ZIF-8 and ferrocene were heated in a tube furnace for 2 h to 150 °C, so that the metal–organic gases were fully captured by ZIF-8, and the precursor was then pyrolyzed at 950 °C. As a gaseous doping precursor, ferrocene significantly reduced the content of oxidation state N, induced the formation of Fe–N_x, and increased the proportion of graphite state N. The C-Fe-ZIF-4.44-950 catalyst with a specific surface area of 1255 $m^2·g^{-1}$ maintained the dodecahedral structure of ZIF-8, and iron was highly dispersed in the catalyst. The catalyst had excellent ORR performance in both acidic and alkaline electrolytes, with electron transfer numbers of 3.97 and 3.98, respectively.

2.4 Preparation of heteroatoms-enhanced Fe–N–C catalysts by MOF carbonization

Heteroatom doping is considered to be an effective method to improve electrochemical performance [47]. For instance, nitrogen atoms can not only improve hydrophilicity, but also change the distribution of charge density in carbon materials, thereby enhancing the catalytic activity. Sulfur can change the spin density, charge density of adjacent carbon atoms, and increase the active area of the material. Owing to the redistribution of charge density and spin density, the co-doping of N and S will produce a synergistic effect. In addition, different N and S sources have different effects on the catalyst. Therefore, according to the type of MOF and catalytic requirements, reasonable heteroatom doping is necessary and can achieve positive effects.

For ZIF, in addition to the necessary Fe source, additional heteroatom doping can effectively enhance the performance of the catalyst. Small molecules or salts containing heteroatoms are common sources of other heteroatoms, such as melamine, NH_3, N_2H_4, $(NH_4)_2S_2O_8$ and NH_4SCN. For example, Chen et al. [36] used melamine as an additive to Fe-ZIF-8 which was prepared by 2-methylimidazole, $Fe(acac)_3$ and $Zn(NO_3)_2 \cdot 6H_2O$, and then pyrolyzed in an Ar atmosphere at 900 °C. The addition of melamine not only increased the N content of Fe@NMC-1 catalyst to 11.82 at%, but also formed more porous network structure. The specific surface area increased from 705.1 to 844.9 $m^2 \cdot g^{-1}$, which was mainly due to the release of gases (such as NH_3) by melamine in the pyrolysis process, which promoted the formation of the inner cavity. Abundant N atoms combined with Fe atoms to form Fe–N_x active sites, which were highly dispersed in a

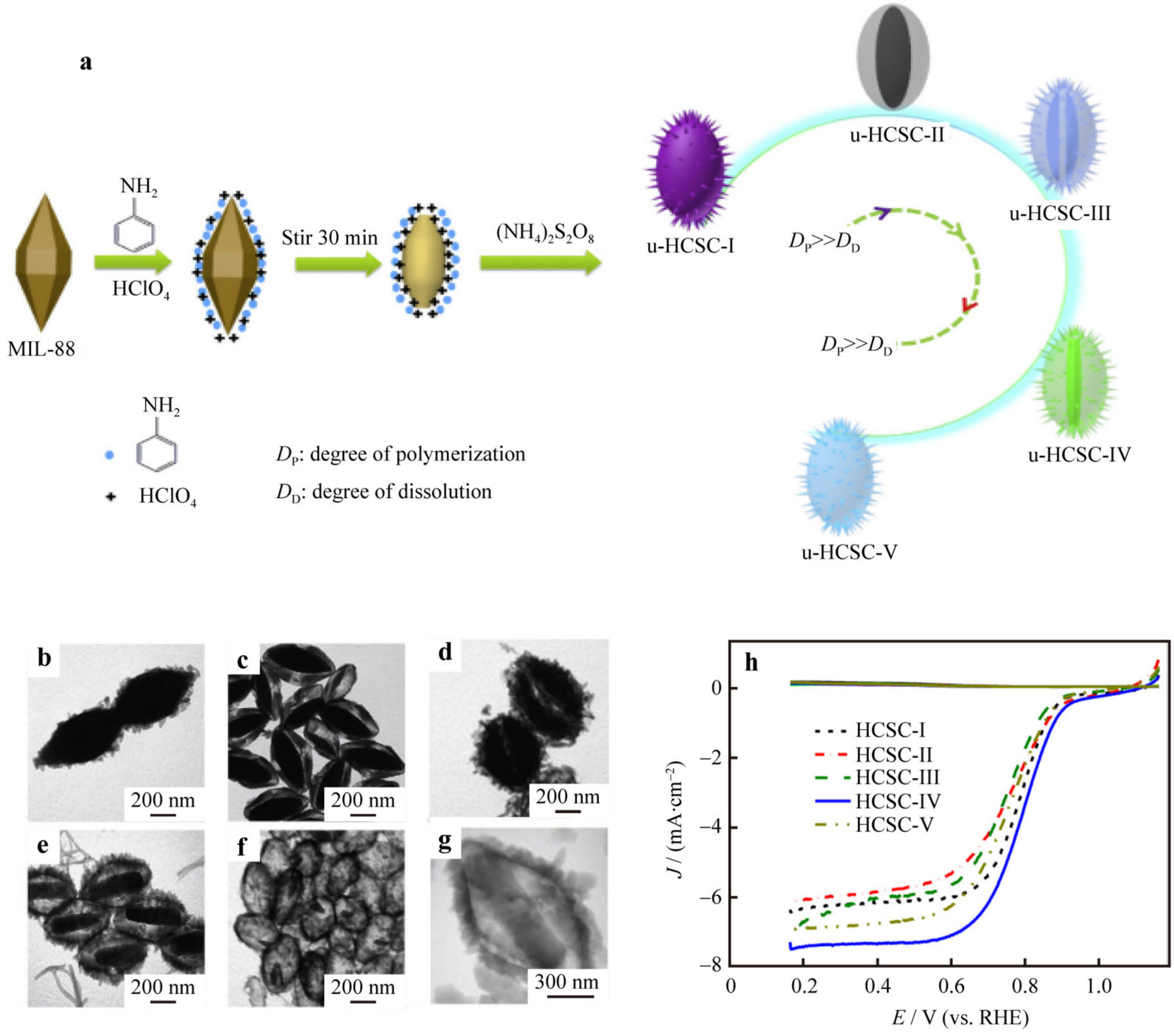

Fig. 4 **a** Schematic illustration of u-HCSC-(I, II, III, IV and V) nanostructures prepared by "polymerization-dissolution" strategy; **b–e** TEM images of u-HCSC-(I, II, III, IV and V) nanostructures; **f–g** HAADF-STEM images of HCSC-IV; **h** polarization curves of materials of different samples in O_2-saturated 0.1 mol·L^{-1} KOH. Reproduced with permission from Ref. [41]. Copyright 2019 Elsevier Ltd

three-dimensional (3D) interconnection network. As a result, the Fe@NMC-1 catalyst exhibited an onset potential of 1.01 V vs. RHE, a half-wave potential of 0.88 V vs. RHE, and a Tafel slope of 54 mV·dec^{-1} in 0.1 mol·L^{-1} KOH (aq.), which was superior to Pt/C catalyst (E_{onset} = 0.97 V (vs. RHE), $E_{1/2}$ = 0.85 V (vs. RHE), Tafel slope = 75 mV·dec^{-1}). Moreover, it showed excellent performance under acidic conditions. Jina et al. [37] mixed ZIF-8, $FeSO_4$, and $N_2H_4·H_2O$ for pyrolysis to prepare a 6% Fe–N–S CNN catalyst with a carbon matrix/nanotube 3D nanostructure (Fig. 3 [37]). $FeSO_4$ provided sources of iron and sulfur. Hydrazine hydrate used as an alkaline reducing agent was effective in preventing the iron oxidation and structural destruction of ZIF-8. The addition of $N_2H_4·H_2O$ not only increased the N content on the catalyst surface, but also promoted the formation of CNTs, which could improve the conductivity of the catalyst, and provide rich channels of the reactants transport. High specific surface area (974 m^2·g^{-1}) and rich Fe and N contents (1.6 at% and 9.65 at%, respectively) were beneficial to forming more Fe–N_x active sites with effective dispersibility. S dopant could also synergistically promote the catalyst's activity. In addition, the in situ formed CNTs increased the conductivity of the catalyst and enriched the electron transport channels. In 0.1 mol·L^{-1} KOH (aq.), the half-wave potential of 6% Fe–N–S CNN catalyst was 0.91 V vs. RHE, higher than that of Pt/C catalyst (0.85 V (vs. RHE)). After 12 h operation, the current density only decreased by 5.21%, indicating that it had good stability.

Owing to its large specific surface area and high stability, MIL is also an alternative precursor [48], which is a framework composed of trivalent transition metal ions (such as Cr^{3+}, Fe^{3+}, Al^{3+}) and carboxylic acid ligands (such as glutaric acid, succinic acid and other dibasic acids). Since these ligands having no N atoms, an additional N source is required in order to prepare the Fe–N–C catalysts from MIL, while the addition of iron source depends on the metal center of MIL. Guo et al. [38] replaced Cr^{3+} with Fe^{3+} and coordinated with 1,3,5-benzenetricarboxylic acid to prepare MIL-101-Fe [49] (832 m^2·g^{-1}), and then encapsulated hexamethylenetetramine (HMT) into the pores of MIL-101-Fe by rotary evaporation. The bottle was under negative pressure when evaporated, which allowed HMT to easily enter the pores of MIL-101-Fe for N loading. When the product was pyrolyzed at 700, 800, 900 and 1000 °C, simple Fe–N_2-700 (128 m^2·g^{-1}), Fe–N_2-800 (138 m^2·g^{-1}), Fe–N_2-900 (151 m^2·g^{-1}) and Fe–N_2-1000 (167 m^2·g^{-1}) were obtained, respectively. However, Fe–N_2-800 showed the outstanding ORR activity with an onset potential of − 0.077 V (vs. SCE) and a half-wave potential of − 0.25 V (vs. SCE), which were close to that of Pt/C catalyst (E_{onset} = −0.033 V (vs. SCE), $E_{1/2}$ = −0.175 V (vs. SCE)). This was because the content of pyridinic-N and graphitic-N was the highest in Fe–N_2-800, and the coexistence of Fe/Fe_3C nanoparticles and Fe–N_x active sites played an important role in promoting ORR activity. Therefore, the proper pyrolysis temperature had a key effect on the performance. Besides, Gao et al. [39] took MIL-101-Fe [50] as the precursor, coated its surface with polyaniline through in situ polymerization, and pyrolyzed it at 900 °C to prepare NC@Fe_3O_4-900-1.5 catalyst with specific surface area of 698.52 m^2·g^{-1}. Polyaniline was not only the source of N, but also could prevent particle aggregation and structure collapse during pyrolysis. Furthermore, it also played an important role in the formation of ORR active sites, such as Fe–N_x and pyridinic-N. The catalyst contained a large number of oxygen-containing groups like –COOH and –OH, and had natural hydrophilicity of C–N bonds (contact angle of 10.6°), which was conducive to the complete entry of aqueous electrolytes into its pores. It exhibited excitation stability with an onset potential of 0.058 V (vs. Hg/HgO), which was close to Pt/C catalyst (0.071 V (vs. Hg/HgO)).

In addition to the doping of N atoms, S doping will also lead to the improved catalyst performance. For instance, Yang et al. [40] mixed MIL-53 [51] (iron ion center), $(NH_4)_2S_2O_8$ and melamine by ultrasonication, then heated the mixture at 240 °C for 2 h and 900 °C for 1 h, and finally obtained the N, S co-doped $Fe_{0.2}N_{0.2}M_{0.2}$-900 catalyst. The Fe, N and S contents of $Fe_{0.2}N_{0.2}M_{0.2}$-900 were 0.62 at%, 3.25 at% and 0.82 at%, respectively. $(NH_4)_2S_2O_8$ is a weak acidic salt. Adding melamine can adjust the pH, which is beneficial to control the morphology of the catalyst. Therefore, $F_{0.2}N_{0.2}M_{0.2}$-900 not only maintained the spindle morphology of the MOF precursor, but also formed the graphene structure, and a large amount of CNTs, which was helpful for electron transfer. The $F_{0.2}N_{0.2}M_{0.2}$-900 catalyst had excellent stability and the measured onset potential (0.970 V (vs. RHE)) and half-wave potential (0.873 V (vs. RHE)) which were higher than those of Pt/C catalyst (0.942 V (vs. RHE) and 0.807 V (vs. RHE), respectively). Besides, Yang et al. [41] prepared the Fe, N, S tri-doped core–shell carbon catalyst (HCSC catalyst) with MIL-88 as the sacrifice template and iron source (Fig. 4 [41]). First, MIL-88, aniline, and $HClO_4$ were stirred in an ice bath for 30 min, then aniline adhered to the surface of MIL-88, while H^+ etched the tip of the MIL-88 polyhedron into an elliptical sphere. An initiator $(NH_4)_2S_2O_8$ was added to induce aniline polymerization to form a porous polyaniline shell on the outer surface of MIL-88. Meanwhile, MIL-88 further dissolved in equilibrium to form a nucleus after sufficient reaction time. In this process, MIL-88 served as a sacrificial template to promote Fe, N, S dispersion in the carbon skeleton. After further pyrolysis at 240 °C for 2 h in N_2 atmosphere, and then at

Table 3 Summary of synthesis of MOF-based Co–N–C catalyst and cobalt oxide catalyst

Sample	Active site	MOF			Lord	Pyrolysis precursor	Pyrolysis conditions	Refs.
		Type	Central ion	Ligand				
Co@NPC-acid	Co–N–C	Co-PPD	$Co(NO_3)_2$	p-phenylenediamine (PPD)	–	Co-PPD	800 °C (Ar, 2 h)	[62]
Co@BNCNTs-900	Co–N	$Co(dca)_2pyz$	$Co(NO_3)_2$	sodium dicyanamide (Na(dca)), pyrazine	–	$Co(dca)_2pyz$	900 °C (10 °C·min^{-1}, N_2, 2 h)	[63]
CoN-CF-700	$Co–N_x$	Co-MOF	Cobalt acetate	2,2′-bipyridyl-5,5′-dicarboxylic acid	–	Co-MOF	700 °C (2 °C·min^{-1}, N_2, 2 h)	[64]
Co@N-CNTF-2	Co–N	Co-Ade-MOF	Cobalt acetate	Adenine	–	Co-Ade-MOF	700 °C (N_2)	[65]
Co_3O_4/HNCP-40	Co_3O_4	ZIF-67	$Co(NO_3)_2$	2-methylimidazole	–	ZIF-67	800 °C (2 °C·min^{-1}, $H_2/Ar = 1/9$, 2 h); 250 °C (2 °C·min^{-1}, O_2/Ar = 3/97, 40 min)	[66]
Co@Co_3O_4/CN-2	Co_3O_4	$Co(atz)(bdc)_{0.5}$	$Co(NO_3)_2$	3-amino-1,2,4-triazole, benzene-1,4-dicarboxylic acid	–	$Co(atz)(bdc)_{0.5}$	700 °C (5 °C·min^{-1}, N_2, 2 h); 250 °C (5 °C·min^{-1}, air, 90 min)	[67]
C-MOF-C2-900	$Co-N_x$ CoO_x	MOF-C2	$Co(NO_3)_2$	1,2,4-benzenetricarboxylic acid, MIDPPA	–	MOF-C2	900 °C (5 °C·min^{-1}, Ar, 1 h)	[68]
Co@C-600	Co/CoO_x	Co-MOF	$Co(NO_3)_2$	Polyvinylpyrrolidone (PVP),1,4 benzenedicarboxylic acid	–	Co-MOF	600 °C (N_2, 5 h)	[69]
$Co_{0.6}$-N/C-800	$Co–N_x$	ZIF-67	$Co(NO_3)_2$	2-methylimidazole	$Zn(NO_3)_2$	$Co_{0.6}Zn_{0.4}$-ZIF	800 °C (2 °C·min^{-1}, N_2, 2 h)	[70]
C3-900-N/S	Co–N, Co–O	Co-MOF	$Co(NO_3)_2$	4,4′-biphenyldicarboxylic acid	$Mg(NO_3)_2$, urea, thiourea	Mg/Co-MOF; C3-600-HCl	Mg/Co-MOF (600 °C, 5 °C·min^{-1}, Ar, 5 h), C3-600-HCl, (900 °C, 10 °C·min^{-1} N_2, 1 h)	[71]
P-Co–NC-4	$Co–N_x$	ZIF-67	$Co(NO_3)_2$	2-methylimidazole	Polyvinylpyrrolidone (PVP)	P-ZIF-67-4	800 °C (5 °C·min^{-1}, N_2, 2 h)	[72]
Single-holed Co/NC hollow particles	Co/NC	ZIF-67	$Co(NO_3)_2$	2-methylimidazole	Polystyrene (PS)	PS@ZIF-67	200 °C (5 °C·min^{-1}, N_2, 2 h), 800 °C (5 °C·min^{-1}, N_2, 2 h)	[73]
Co-HNCS-0.2	$Co–N_x$	ZIF-67	$Co(NO_3)_2$	2-methylimidazole	PS, $Zn(NO_3)_2$·	PS@$Zn_{1-x}Co_x$-ZIF	900 °C (5 °C·min^{-1}, N_2, 4 h)	[74]
Co–N–C/rGO-6-600	Co–N CoO_x	Co-MOF	Cobalt acetate	2-methylimidazole	Graphene oxide (GO)	Co-MOF/GO-6	600 °C (10 °C·min^{-1}, N_2, 5 h)	[75]
Co_3O_4/Co@N-G-450	N-doped Co_3O_4/Co	ZIF-67	$Co(NO_3)_2$	2-methylimidazole, polyvinylpyrrolidone, triethylamine	Exfoliated graphene oxide (EGO)	ZIF-67@EGO	450 °C (5 °C·min^{-1}, N_2, 6 h)	[76]
MOF(Co)/C(3:1)-500	Co–CoO_x	MOF(Co)	$Co(NO_3)_2$	3,5-dimethyl-4-carboxypyrazole	Carbon black (CB, Vulcan XC-72)	MOF(Co) and CB	500 °C (N_2, 2 h)	[77]

Table 3 continued

Sample	Active site	MOF				Pyrolysis precursor	Pyrolysis conditions	Refs.
		Type	Central ion	Ligand	Lord			
Co, N-PCL(4)	Co–N_x	ZIF-L	$Zn(NO_3)_2$	2-methylimidazole	ZIF-67	ZIF-L@ZIF-67	800 °C 2 °C·min^{-1}, N_2, 5 h	[78]
Co@CN	Co–N–C	Mg-MOF	$MgNO_3$	1,4-naphthalene dicarboxylic acid (ndc)	5,10,15,20-tetrakis (4-methoxyphenyl)-21H, 23H-porphine cobalt (II) complex	NCD-1 + cobalt (II) complex	NCD (200 °C, Ar, 6 h); Co@CN (800 °C, N_2, 2 h)	[79]

800 °C for 1 h, a porous core–shell HCSC-IV catalyst with a specific surface area of 90.5 $m^2 \cdot g^{-1}$ and an I_D/I_G ratio of 0.93 was obtained. The special nucleus of HCSC was similar to the vein of a leaf and was important to the electrocatalytic process by facilitating charge transfer to the entire shell nanostructure. Hence, the catalyst exhibited an onset potential of 0.918 V (vs. RHE), a half-wave potential of 0.794 V (vs. RHE), a diffusion limiting current density of 7.35 $mA \cdot cm^{-2}$, and good stability.

Other types of MOF can also be used as precursors of Fe–N–C catalysts by heteroatom doping. For instance, Huang et al. [42] prepared porous carbon-containing copper nanoparticles (Cu@PC) by using Hong Kong University of Science and Technology-1 MOF (HKUST-1) as precursor and pyrolyzed at 800 °C for 2 h. Cu@PC was dispersed in saturated $FeCl_3$ aqueous solution, and copper particles were etched to obtain porous carbon (PC). PC was further mixed with FePC, and then annealed in ammonia gas to obtain the Fe_2N@NPC-500 catalyst (381 $m^2 \cdot g^{-1}$). The uniform distribution of Fe_2N nanoparticles and their close contact with the shell promoted the formation of Fe–N/C bond and the increase of active sites. Owing to the uniform distribution of NPs, large specific surface area, large number of mesopores and active Fe–N/C binding, Fe_2N@NPC-500 catalyst showed an onset potential of − 0.038 V (vs. Ag/AgCl), and a half-wave potential of − 0.175 V (vs. Ag/AgCl), which was close to commercial Pt/C catalyst. In addition, the stability of the catalyst was higher than that of Pt/C catalyst. Zheng et al. [43] encapsulated the hydrophilic NH_4SCN and $FeCl_3$ into the University of Oslo-66-NH_2 MOF (UIO-66-NH_2) by a double-solvent method, making Fe and S highly dispersed in the derived carbon. Compared with the impregnation method, the double-solvent method realized the atomic-level dispersion of active sites on the mesoporous structure and maintained the form of derived carbon, which was beneficial to the catalytic performance of the MOF-derived carbon catalyst. The resulting carbon material perfectly inherited the morphology of UIO-66-NH_2 precursor, forming large surface area, clear mesoporous structure and atomic dispersion of doped elements. After heating, the I_D/I_G ratio of the Fe/N/S-PC catalyst was 1.19, indicating that there were more carbon defects in the catalyst and more active sites were exposed. Moreover, the addition of S can reduce the content of oxidized-N (10.71%), increase the content of pyridinic-N (19.49%), metal-N (9.11%) and graphitic-N (45.64%). Pyridinic-N can activate the ORR process and reduce ORR overpotential, while the presence of graphitic-N facilitates electron conduction and increases the catalytic current of ORR [52, 53]. Fe/N/S-PC contained 0.31 at% iron, 4.93 at% nitrogen, 1.49 at% sulfur, and high specific surface area (1589 $m^2 \cdot g^{-1}$) as well high porosity (77.22%), resulting in excellent ORR performance in

Table 4 Summary of ORR electrocatalytic activities of MOF-based Co–N–C catalyst and cobalt oxide catalyst

Catalyst	Co content	Hetero⁻ atom content	I_D/ I_G	S_{BET}/ ($m^2 \cdot g^{-1}$)	Catalyst loading/ ($m^2 \cdot g^{-1}$)	Electrolyte (0.1 $mol \cdot L^{-1}$)	E_{onset}/V (vs. RHE)	$E_{1/2}$/V (vs. RHE)	Tafel slope/ ($mV \cdot dec^{-1}$)	*n*	H_2O_2 yield/%	Refs.
Co@NPC-acid	1.72 wt%	–	–	859.50	0.200	KOH	–	0.120 (vs. Hg/HgO)	–	3.95	3.0	[62]
Co@BNCNTs-900	0.45 at%	2.09 at% N	0.92	147.08	0.300	KOH	0.930	0.820	–	3.91–4.01	12.0	[63]
CoN-CF-700	3.73 at%	4.13 at% N	1.08	593.10	0.200	KOH	0.940	0.850	–	3.95	4.0	[64]
Co@N-CNTF-2	5.80 at%	6.50 at% N	1.00	214.30	0.280	KOH	0.910	0.810	47.6	3.96	–	[65]
Co_3O_4/HNCP-40	39.38 wt%	7.16 wt% N	–	204.00	0.204	KOH	–	0.834	69.0	3.90	6.0	[66]
Co@Co_3O_4/CN-2	–	–	1.00	78.27	0.250	KOH	–	0.150 (vs. Ag/AgCl)	–	~ 3.90	~ 6.0	[67]
C-MOF-C2-900	1.20 at%	0.70 at% N, 5.20 at% O	1.22	265.00	0.200	KOH	–	0.820	–	3.80–4.00	–	[68]
Co@C-600	3.90 at%	10.50 at% O	3.21	96.80	0.250	KOH	0.870	–	–	~ 4.00	–	[69]
$Co_{0.6}$-N/C-800	5.40 at%	4.10 at% N	1.51	283.20	0.254	KOH	0.916	0.825	77.0	3.85	~ 20.0	[70]
C3-900-N/S	–	2.07 at% N, 5.80 at% S	1.06	465.63	~ 0.300	KOH	~ 0.800	–	–	3.91	4.5	[71]
P–Co–NC-4	–	1.88 at% N	1.08	548.00	0.400	KOH	0.900	0.850	–	3.49–3.89	~ 10.0	[72]
Single-holed Co/NC hollow particles	–	–	–	–	0.250	KOH	0.980	0.870	102.0	3.99	–	[73]
Co-HNCS-0.2	18.64 wt%	5.92 wt% N	0.95	734.40	0.100	KOH	0.940	0.820	76.0	3.96	8.0	[74]
Co–N–C/rGO-6-600	0.37 at%	–	0.99	252.00	–	KOH	0.963	0.870	54.0	3.74–3.98	–	[75]
Co_3O_4/Co@N-G-450	1.07 at%	3.80 at% N 10.36 at% O	–	–	0.280	KOH	0.962	0.808	62.0	3.91–3.96	–	[76]
MOF(Co)/C(3:1)-500	–	–	–	203.50	0.240	KOH	0.920	0.800	51.0	3.91–3.98	–	[77]
Co, N-PCL(4)	–	–	–	319.00	0.200	KOH	–	0.846	48.7	3.96–3.99	–	[78]
Co@CN	1.50 wt%	–	0.87	–	0.198	KOH	0.800	–	–	–	2.3	[79]

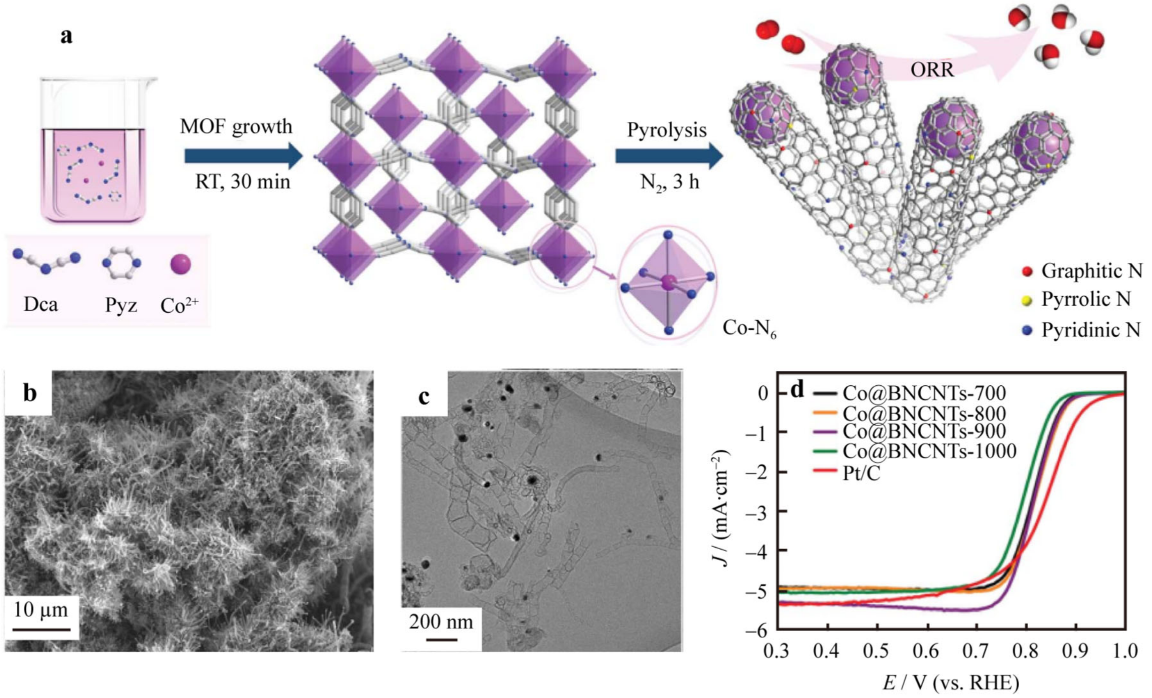

Fig. 5 **a** Schematic illustration of preparation of Co@BNCNTs as an electrocatalyst for oxygen reduction reaction; **b** SEM and **c** HRTEM images of Co@BNCNTs; **d** LSV curves of Co@BNCNTs-700, 800, 900, 1000 and Pt/C in O_2-saturated 0.1 mol·L^{-1} KOH (aq.). Reproduced with permission from Ref. [63]. Copyright 2018 Royal Society of Chemistry

acidic or alkaline electrolyte. The large specific surface area was mainly credited to the addition of Fe, which played an important role in the formation of mesoporous structure and porosity. In 0.1 mol·L^{-1} KOH (aq.), Fe/N/S-PC catalyst exhibited an onset potential of 0.97 V (vs. RHE) and a half-wave potential of 0.87 V (vs. RHE). It was superior to Pt/C (E_{onset} = 0.94 V (vs. RHE), $E_{1/2}$ = 0.84 V (vs. RHE)). In 0.1 mol·L^{-1} $HClO_4$ (aq.), it showed an onset potential and a half-wave potential of 0.89 V (vs. RHE) and 0.785 V (vs. RHE), respectively, and followed the 4-electron mechanism. In conclusion, as long as the methods and strategies are reasonable and appropriate, various heteroatom sources and doping methods can use different types of MOF as precursors for catalysts preparation.

2.5 Summary of MOF-based Fe–N–C catalyst

The electrochemical properties of catalysts are determined by a variety of factors, such as the structure and dispersion of active sites, specific surface area, porosity, conductivity and hydrophilicity. Therefore, the influence of precursor structure and heat treatment method on Fe–N–C catalyst is very crucial. The direct carbonization of Fe-MOF to prepare Fe–N–C catalyst has the following advantages: (1) The target structure of MOF can be designed from cheap iron sources and organic ligands; (2) Fe-MOF precursor has high iron content and atom dispersibility, which is beneficial to obtaining highly dispersed Fe–N_x active sites; (3) One-pot preparation and one-step pyrolysis are relatively simple. However, in order to avoid structural collapse and particle aggregation during pyrolysis, the Fe-MOF structure needs to be finely designed.

By selecting suitable MOF carrier to load the iron source, Fe–N–C catalyst with high performance can also be prepared. The specific surface area, pore size and coordination number of MOF are the focus of adjustment. The porous network structure and proper aperture of MOF enable Fe ions to penetrate easily and bind to abundant coordination sites (such as N) for in situ loading. The iron source can be selected according to the characteristics of the carrier, such as molecular size and chemical properties. The chemical adsorption method is mainly used to achieve a stable load. By adjusting the ratio of MOF to iron source, pyrolysis temperature, atmosphere and time, the optimal loading effect and ORR catalytic activity can be achieved.

The Fe–N–C catalysts prepared by doping different heteroatoms can effectively improve the morphology after pyrolysis, thus promoting ORR catalysis, especially for N-free MOF precursors. At present, the most common heteroatom doping is mainly electronegative atoms (such as N) or larger-size atoms (such as S). The advantages of heteroatom doping are: (1) the heteroatom raw materials, such as melamine and polyaniline, are very cheap; (2) the

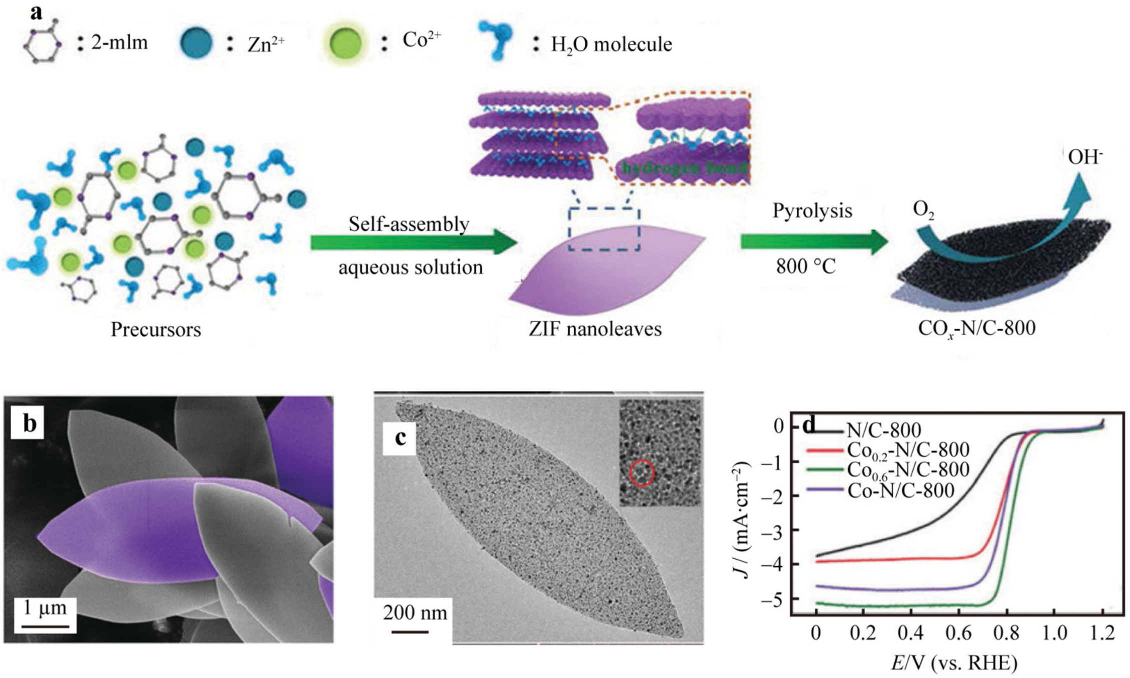

Fig. 6 **a** Schematic illustration of synthesis process of ZIF nanoleaves in aqueous solution and its subsequent conversion to Co_x-N/C nanoleaves; **b** SEM image of $Co_{0.6}Zn_{0.4}$-ZIF nanoleaves; **c** TEM image of $Co_{0.6}$-N/C-800 (inset: magnification image of red marked area; typical pore structure is marked by red circle); **d** LSV curves of N/C-800, $Co_{0.2}$-N/C-800, $Co_{0.6}$-N/C-800 and Co–N/C-800. Reproduced with permission from Ref. [70]. Copyright 2019 Royal Society of Chemistry

heteroatom source is easy to compound, with obvious doping effect, which can effectively improve the ORR effect; (3) under controllable reaction conditions, the optimal element ratio can be adjusted by the ratio of MOF precursor to additive.

3 MOF-based Co–N–C catalyst and cobalt oxide catalyst

3.1 Introduction of MOF-based Co–N–C catalyst and cobalt oxide catalyst

Owing to excellent electrochemical performance, Co–N–C catalysts and Fe–N–C catalysts have been widely studied to replace noble metal catalyst of ORR [54]. Similar to Fe–N–C catalyst, the active center of Co–N–C catalyst is mainly Co–N_x [55]. Yan et al. [56] found that the atomic Co with tetrahedral coordination played an extremely important role in the ORR process. In addition, the effect of metallic Co NPs on the activity of Co–N–C catalyst was also studied. Zhao et al. [57] found that Co NPs coating on the catalyst surface and carbon layer had little effect on the activity of catalyst and even affected the high yield of H_2O_2. Therefore, it is of great significance to pyrolyze the cobalt ions in the precursor into active sites that are favorable for catalysis rather than cobalt metal particles.

Cobalt oxide, including Co_3O_4 and CoO with a rock-salt structure, has been reported to have ORR catalytic activity [58, 59]. Owing to the good dispersibility of cobalt oxide particles and favorable conductivity of catalysts, the activity can be effectively improved by combining cobalt oxide with the carbon matrix. CoO and Co_3O_4 were used as active centers to prepare high-performance catalysts. For example, Liu's group [60] studied the effect of the geometric occupancy and oxidation state of cations in cobalt oxide on ORR activity. They found that the Co^{2+} $\left(\mathrm{Co}_{\mathrm{Oh}}^{2+}\right)$ and Co^{3+} in the octahedral site $\left(\mathrm{Co}_{\mathrm{Oh}}^{3+}\right)$ were the main active sites of CoO and Co_3O_4, respectively; while the activity of $\left(\mathrm{Co}_{\mathrm{Oh}}^{2+}\right)$ was higher than that of $\left(\mathrm{Co}_{\mathrm{Oh}}^{3+}\right)$. In the ORR, the $\left(\mathrm{Co}_{\mathrm{Oh}}^{2+}\right)$ sites in CoO tended to be converted into $\left(\mathrm{Co}_{\mathrm{Oh}}^{3+}\right)$ and Co_3O_4 was formed, indicating that the reaction was unstable. Therefore, the corresponding cobalt oxide catalyst can be prepared by MOF pyrolysis for different active sites.

3.2 Preparation of Co–N–C catalyst and cobalt oxide catalyst by carbonization of Co-MOFs

Co-MOFs can be prepared by different cobalt compounds and organic ligands. For example, by solvothermal method, $Co(NO_3)_2 \cdot 6H_2O$ and 2-methylimidazole can prepare ZIF-67 with rhombic dodecahedron structure with large specific surface area [61]. Liu et al. [62] took p-phenylenediamine (PPD) as the organic ligand and $Co(NO_3)_2$ to prepare the rosette spherical Co-PPD complex composed of cross-linked slices through simple hydrothermal reaction (Table 3 [62–79]). After pyrolysis in an Ar atmosphere at 800 °C for 2 h, some Co ions were reduced to Co(0) and diffused into the graphene shell, thus producing a Co@NPC-acid catalyst with 1.72 wt% Co (Table 4 [62–79]). The inert substances on the catalyst surface, such as cobalt oxide and cobalt, can be removed by soaking in an acidic solution for activation. Meanwhile, compared with non-acid-etched Co@NPC (specific surface area: 242.6 $m^2 \cdot g^{-1}$; pore volume: 0.34 $cm^3 \cdot g^{-1}$), Co@NPC-acid had a larger contact area (859.5 $m^2 \cdot g^{-1}$, 1.82 $cm^3 \cdot g^{-1}$), which provided more opportunities for the contact between active sites and reactive substances. In 0.1 $mol \cdot L^{-1}$ KOH (aq.), the half-wave potential of Co@NPC-acid catalyst with Co–N_x active sites was 0.12 V vs. Hg/HgO, and the diffusion limiting current density was 5.3 $mA \cdot cm^{-2}$, which was higher than that of Pt/C catalyst. After 10 h of continuous testing, the Co@NPC-acid catalyst maintained 91% of the initial current, showing excellent stability. Ma et al. [63] prepared rod-shaped Co-MOF using sodium dicyandiamide, pyrazine and $Co(NO_3)_2$ (Fig. 5 [63]). Dicyandiamide was used as carbon and nitrogen source for Co-MOF pyrolysis in a N_2 atmosphere at 900 °C for 2 h to induce the formation of graphite structures. The prepared Co@BNCNT-900 catalyst had high-density bamboo-like N-doped CNT structures, which was beneficial to improve conductivity and provide accessible active sites. The onset and half-wave potentials of the Co@BNCNT-900 catalyst was 0.93 V (vs. RHE) and 0.82 V (vs. RHE), respectively. The electron transfer number was 3.9, which proved the excellent ORR activity. In addition, Xu et al. [64] selected 2,2′-bipyridyl-5,5′-dicarboxylic acid (H2bpydc) and cobalt acetate to synthesize the Co-MOF precursor. In the carbonization process, H2bpydc would release CO_2 and H_2O, forming mesoporous N-doped graphitic carbon layer. At the same time, cobalt tetrahydrate was reduced to metallic cobalt NPs that coordinated with graphite carbon, and it was embedded into 3D N-rich mesoporous carbon foam, exposing more active sites. After pyrolysis at 700 °C in N_2 atmosphere, the obtained CoN-CF-700 catalyst contained 3.73 at% Co, 4.13 at% N and the BET specific surface area

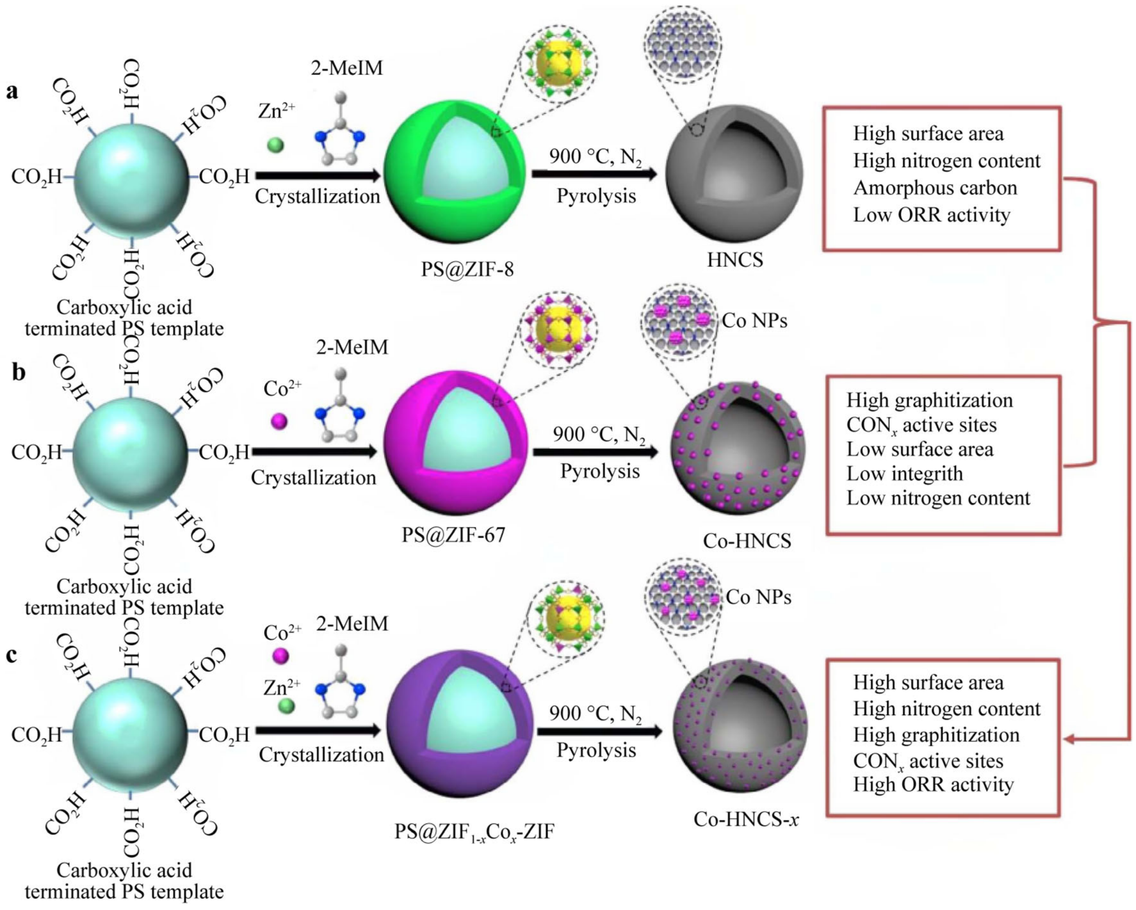

Fig. 7 Schematic illustration of procedures for synthesis of **a** HNCS, **b** Co-HNCS, and **c** Co-HNCS-x. Reproduced with permission from Ref. [74]. Copyright 2017 Elsevier B.V.

was 593 $m^2 \cdot g^{-1}$. The core–shell structure of Co NPs coated with graphitic carbon layer had unique structural advantages, which not only improved ORR performance through physical and chemical protection, but also played a role in the conduction pathway and reaction site in the electrocatalysis process. CoN-CF-700 catalyst also displayed an onset potential of 0.94 V (vs. RHE), and a half-wave potential of 0.85 V (vs. RHE). Besides, the core–shell structure of Co NPs enclosed by graphitic carbon layers can reduce the corrosion of active sites and play a long-term stabilizing role in ORR catalysis.

In addition to traditional organic ligands, biomass ligands can also coordinate with Co^{2+} to construct Co-MOF. Guo et al. [65] used adenine, a biomass material with high N content (51.8%) and rigid molecular structure, to prepare Co-Ade-MOF with cobalt/adenine molar ratio of 1/3. It was further pyrolyzed at 700 °C in N_2 atmosphere to obtain Co@N-CNTF-2 catalyst. The Co-MOF was synthesized by adenosine ligands and pyrolyzed without any other precursors to form a N-doped carbon/CNT skeleton containing Co NPs. On the one hand, Co NPs not only catalyzed the formation of CNTs and hollow carbon structures, but also improved the conductivity of the entire hybrid structure. On the other hand, less graphitized shells can prevent the acid corrosion, oxidation and aggregation of Co NPs during electrocatalysis, especially under the high oxidation potential of strong acidic electrolyte, so that Co NPs had good durability and stability in harsh environments. The Co-doped carbon core–shell structure provided an effective way to adjust the electronic structure of the catalyst, thus greatly reducing the adsorption free energy and local work function, and promoting the adsorption and desorption of reaction intermediates. The N content of the prepared catalyst was 6.5 at%, in which pyridinic-N and graphitic-N accounted for 90%, indicating high catalytic activity. The pore size was about 0.5 nm, which facilitated the efficient transport of electrolyte ions and gaseous substances. Therefore, in 0.1 $mol \cdot L^{-1}$ KOH (aq.), Co@N-CNTF-2 catalyst exhibited an onset potential of 0.91 V (vs. RHE), and a half-wave potential of 0.81 V (vs. RHE), which was close to that of Pt/C catalyst. The electron transfer number was 3.96, indicating its admirable ORR activity.

For cobalt oxide catalyst, the Co-MOF precursor requires a mild pyrolysis temperature, because cobalt oxide can be reduced by carbon at high temperatures. Secondly, compared with Co–N–C catalyst, the pyrolysis atmosphere needs a certain amount of O_2, which is conducive to the formation of active sites. Ding et al. [66] prepared Co_3O_4 NPs by two-step pyrolysis with ZIF-67 as the precursor. The pyrolysis of ZIF-67 in H_2/Ar (H_2:Ar = 1:9) at 800 °C produced the Co NPs. Then, Co NPs were oxidized at 250 °C for 40 min under O_2/Ar atmosphere (O_2:Ar = 3:97). They were finally converted into yolk@shell Co@Co_3O_4 NPs and a small amount of hollow Co_3O_4 NPs through the nanoscale Kirkendall effect. The oxidation time had an important influence on the morphology and structure of the products. When the oxidation time reached 90 min, all Co_3O_4 NPs were converted into hollow Co_3O_4 NPs. With the change of the oxidation time, the specific surface area of the product decreased from 246 $m^2 \cdot g^{-1}$ (no oxidation) to 176 $m^2 \cdot g^{-1}$ (with 90 min oxidation). The optimized yolk@shell Co@Co_3O_4 NPs had the following advantages: (1) Large surface area increased the density of exposed active sites and accelerated the charge transfer; (2) With good dispersive yolk@shell Co@Co_3O_4 NPs, the high electrochemical activity and structural stability were obtained; (3) There were enough N species as supplementary active sites for ORR and hollow porous carbon shells, which can improve conductivity, promote electron transfer and mass diffusion. In 0.1 $mol \cdot L^{-1}$ KOH (aq.), the half-wave potential of Co_3O_4/HNCP-40 catalyst for 40 min of oxidation was 0.843 V relative to RHE, the Tafel slope was 69 $mV \cdot dec^{-1}$, and the diffusion limiting current density was 5.88 $mA \cdot cm^{-2}$. It was close to commercial Pt/C catalyst ($E_{1/2}$ = 0.84 V (vs. RHE), J_L = 5.81 $mA \cdot cm^{-2}$). This was mainly due to the excellent electrochemical activity provided by highly dispersed yolk@shell Co@Co_3O_4 NPs, and the high conductivity provided by the hollow N-doped porous carbon, resulting in excellent ORR activity. Qi et al. [67] prepared the $Co(ATZ)(BDC)_{0.5}$ precursor from 3-amino-1,2,4-triazole (ATZ), 4-dicarboxylic acid (BDC) and $Co(NO_3)_2 \cdot 6H_2O$. The Co@Co_3O_4/NC-2 catalyst was prepared by the pyrolysis of $Co(ATZ)(BDC)_{0.5}$ precursor in N_2 at 700 °C for 2 h, and in air atmosphere at 250 °C for 1.5 h. During heat treatment, the Co ions from the MOF framework were easily transformed into metallic Co NPs, which could catalyze organic ligands to form N-doped graphitic carbon layers. When CoNC-700 was further oxidized in air at 250 °C, Co NPs in CoNC-700 were gradually oxidized to Co_3O_4. Co@Co_3O_4/NC-2 had abundant micropores and mesopores, with a specific surface area of 78.27 $m^2 \cdot g^{-1}$. During the ORR process, the layered microporous/mesoporous structure facilitated the transport of reactants/electrolytes and adequate exposure of active sites. In 0.1 $mol \cdot L^{-1}$ KOH (aq.), the Co@Co_3O_4/NC-2 catalyst showed a half-wave potential of 0.15 V relative to Ag/AgCl, and the H_2O_2 yield was less than 6%, representing a 4-electron reaction. Besides, Zhang et al. [68] rationally designed a new enantiotopic 3D MOF-C2 from N-(4-(1H-imidazol-1-yl)phenyl)-4-(pyridin-4-yl)-N-(4-(pyridin-4-yl)phenyl)aniline (MIDPPA), $Co(NO_3)_2 \cdot 6H_2O$ and 1,2,4-benzenetricarboxylic acid. The C-MOF-C2-900 catalyst with graded rod-like structure can be obtained by pyrolyzing MOF-C2 in N_2 atmosphere at 900 °C for 1 h, which contained a series of ORR active Co

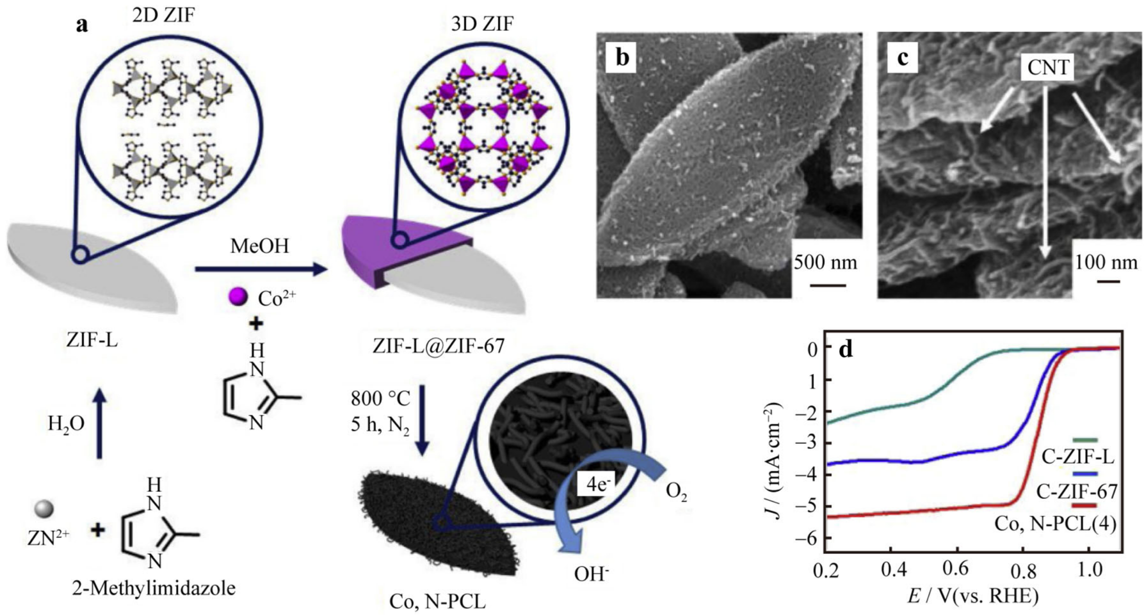

Fig. 8 **a** Schematic representation for formation of leaf-shape ZIF-L and leaf-shape core–shell type ZIF-L@ZIF-67, and its transformation to thin Co, N-PCL; **b**, **c** SEM images of Co, N-PCL (4); **d** LSV in O_2-saturated 0.1 mol·L^{-1} KOH electrolyte of C-ZIF-L, C-ZIF-67 and Co, N-PCL (4). Reproduced with permission from Ref. [78]. Copyright 2019 Elsevier B.V.

sites, such as Co(0), Co–N$_x$ and CoO$_x$. The catalyst showed a half-wave potential of 0.82 V (vs. RHE), which was higher than that of Pt/C catalyst (0.817 V (vs. RHE)). Meanwhile, it showed good stability and methanol resistance, indicating good ORR catalytic activity. Li et al. [69] mixed $Co(NO_3)_2 \cdot 6H_2O$ with polyvinylpyrrolidone (PVP), and added 1,4-benzenedicarboxylic acid (H2bdc) to hydrothermal synthesis of Co-MOF. Then, it was pyrolyzed at 600 °C in N_2 for 5 h to yield Co@C catalyst containing Co/CoO$_x$ NPs. When the pyrolysis temperature increased from 600 to 900 °C, the average size of Co/CoO$_x$ NPs changed from 25 nm to over 100 nm, while the specific surface area of Co@C decreased from 96.8 to 44.1 m^2·g^{-1}, and the atomic ratio of Co(0):Co^{2+}:Co^{3+} changed from 0.32:0.35:0.33 to 0.18:0.42:0.46. The Co@C-600 catalyst was prepared at an optimum temperature of 600 °C. In 0.1 mol·L^{-1} KOH (aq.), the onset potential of Co@C-600 catalyst (vs. RHE) was 0.87 V, and the diffusion limiting current density was 4.9 mA·cm^{-2}, which proved its good ORR performance. In a word, by controlling the structure and pyrolysis conditions of Co-MOF precursor, an excellent cobalt oxide catalyst can be obtained.

3.3 Preparation of heteroatoms-enhanced Co–N–C catalyst and cobalt oxide catalyst by carbonization of Co-MOFs

Encapsulation of small or large molecules into the MOF precursor will cause some changes in the final structure of the catalyst, which affects the catalytic performance. In addition to some commonly used small molecule dopants (such as melamine and ammonium sulfate), vaporizable metal ions, such as Zn^{2+} or Mg^{2+} can also be used as dopants to modify ZIF-67, because Zn and Co have the same coordination number for 2-methylimidazole [80]. Li et al. [70] reported a variety of self-assembled bimetallic ZIF ($Co_{0.6}Zn_{0.4}$-ZIF) in aqueous solution. The 2D stable network was formed by the H-bonds between N atoms in 2-methylimidazole and H_2O (Fig. 6 [70]). Through the coordination of metal ions with 2-methylimidazole, these 2D networks were connected layer by layer to form ZIF nanoleaves. Owing to the same size and coordination number of Co and Zn atoms, the morphology of ZIF nanoleaves was not damaged. The $Co_{0.6}$-N/C-800 catalyst with optimum content of pyridinic-N and graphitic-N was synthesized by pyrolysis in a N_2 atmosphere at 800 °C for 2 h, and retained the lateral size around 3 μm and thickness of about 160 nm. In addition, by adjusting the molar ratio of Co and Zn, a series of N/C-800 (924.7 m^2·g^{-1}, 0.553 cm^3·g^{-1}), $Co_{0.2}$-N/C-800 (311.8 m^2·g^{-1}, 0.244 cm^3·g^{-1}), $Co_{0.6}$-N/C-800 (283.2 m^2·g^{-1}, 0.421 cm^3·g^{-1}), Co–N/C-800 (179.1 m^2·g^{-1}, 0.377 cm^3·g^{-1}) with different specific surface area and pore volume were available. This result indicated that Zn vaporization could prevent the damage of micropores in ZIF. However, among the four samples, $Co_{0.6}$-N/C-800 had the most excellent ORR performance, indicating that cobalt doping could effectively enhance the activity of the catalyst while the proper pores were

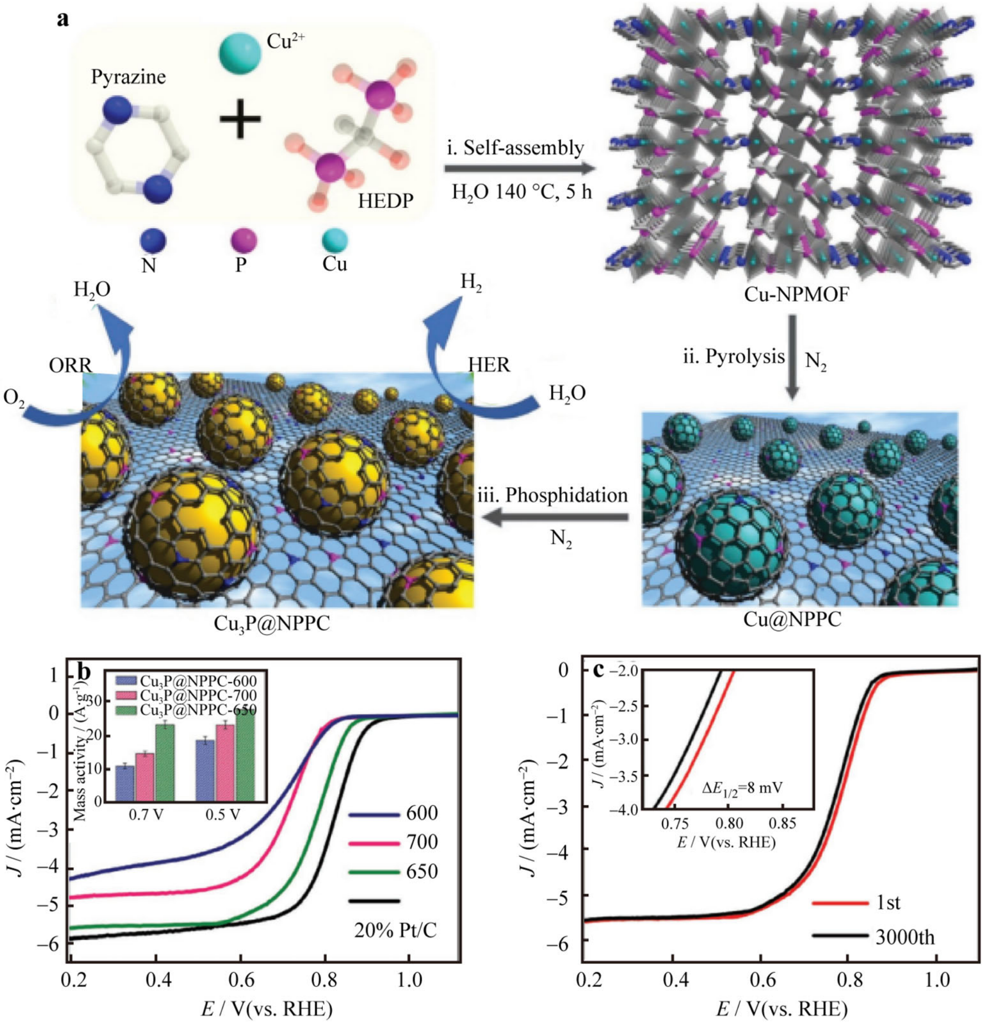

Fig. 9 **a** Schematic illustration of preparation of Cu_3P@NPPC; **b** LSV curves of Cu_3P@NPPC-600, 650, 700 and Pt/C in O_2-saturated 0.1 mol·L^{-1} KOH solution, inset being corresponding mass activities and error bar of Cu_3P@NPPC catalyst; **c** endurance test of Cu_3P@NPPC-650 catalyst. Reproduced with permission from Ref. [84]. Copyright 2017 Wiley–VCH

necessary. In 0.1 mol·L^{-1} KOH (aq.), $Co_{0.6}$-N/C-800 catalyst exhibited an onset potential of 0.916 V (vs. RHE) and a half-wave potential of 0.825 V (vs. RHE), which were comparable to that of Pt/C catalyst ($E_{\mathrm{onset}} = 0.926$ V (vs. RHE) and $E_{1/2} = 0.811$ V (vs. RHE)). These results revealed that the $Co_{0.6}$-N/C-800 catalyst had excellent ORR activity, which was mainly attributed to the rapid mass transfer of the 2D porous foliation structure and abundant active site exposure. Therefore, by adjusting the ratio of Co and Zn in ZIF, catalysts with different properties can also be produced. Since non-toxic and low-cost MgO residue could be simply removed by acid or high-temperature evaporation, Mg was also widely used as a sacrificial agent. For instance, Wu et al. [71] introduced light metal Mg to synthesize Mg–Co bimetallic MOF, and then pyrolyzed at 600 °C. The BET surface of the CNT-containing nanoporous carbon was 712.78 m^2·g^{-1}, much larger than that of the Co-MOF (305.4 m^2·g^{-1}). After post-synthetic modification with N/S heteroatoms at 900 °C, the resulting hierarchical carbon catalyst showed higher activity in ORR than the commercial Pt/C catalyst.

Moreover, large molecules like PANI, PVP, PS, graphene are also commonly used additives. According to the expected catalyst effects, such as improved surface roughness and conductivity, Co-MOF and large molecules can be targeted to increase activity. For instance, Liang et al. [72] prepared Co-embedded N-enriched meso/microporous carbon materials through the auxiliary pyrolysis of ZIF-67 wrapped by PVP. The addition of PVP was beneficial to the increase of the N content and the formation of the interface structure, thus further promoting the enhancement of ORR activity. The C=O group in PVP had a strong coordination effect with the metal center of ZIF-67, which prevented the disintegration of ZIF-67 during

Table 5 Summary of synthesis of MOF-based non-noble metal (Cu, Mn, Ni, Mo) catalysts

Sample	Active site	MOF			Lord	Pyrolysis precursor	Pyrolysis conditions	Refs.
		Type	Central ion	Ligand				
Cu_3P@NPPC-650	Cu_3P	Cu–NPMOF	$Cu(NO_3)_2$	1-hydroxyethylidene-1,1-diphosphonic acid, pyrazine	$NaH_2PO_2 \cdot H_2O$	Cu–NPMOF	650 °C (10 °C·min^{-1}, N_2, 4 h)	[84]
CuNC/KB-400	Cu/Cu_2, CuN_xC_y	Cu-MOF	$Cu(NO_3)_2$	1,4-benzenedicarboxylic acid, triethylenediamine	Carbon support KB (Ketjenblack carbon, EC-300 J)	Cu-MOF/KB	800 °C (5 °C·min^{-1}, Ar, 1 h)	[85]
Cu–N/C	Cu(II)–N	ZIF-8	$Zn(NO_3)_2$	2-methylimidazole	$CuCl_2$	Cu@ZIF-8	1000 °C (5 °C·min^{-1}, Ar/H_2, 3 h)	[86]
25% Cu–N/C	N–Cu(II)–Cu^0	ZIF-8	$Zn(NO_3)_2$	2-methylimidazole	$Cu(NO_3)_2$	Cu-ZIF-8	900 °C (2 °C·min^{-1}, N_2, 2 h)	[87]
Ni@NiNC-600	Ni–N	FA-Ni	$Ni(NO_3)_2$	Folic acid	–	FA-Ni	600 °C (2 °C·min^{-1}, N_2, 2 h)	[88]
Ni-NSPC-6	Ni_3S_2	Ni-NSMOF	Nickel acetate	2-mercapto-5-methyl-1,3,4-thiadiazole	–	Ni-NSMOF	400 °C (2 °C·min^{-1}, Ar/H_2 = 95/5, 1 h), 700 °C (3 h)	[89]
Ni-GT-750-A	Ni/Ni_xS_y	Ni-GT	$Ni(NO_3)_2$	Guanidine thiocyanate (GT)	–	Ni-GT	750 °C (10 °C·min^{-1}, N_2, 3 h)	[90]
MnO@NC-1100	MnO	$Cd_3Mn(L)_2(OH)_2(H_2O)_2$	$CdCl_2$, $MnCl_2$	5′-(4-(1H-tetrazol-5-yl)-benzamido)-benzene-1,3-dioic acid	–	$Cd_3Mn(L)_2(OH)_2(H_2O)_2$	1100 °C (3 °C·min^{-1}, Ar, 2 h)	[91]
Mn_3O_4@NCP	Mn_3O_4	ZIF-8	$Zn(NO_3)_2$	2-methylimidazole	Manganese nitrate	ZIF-8	900 °C (3 h)	[92]
Mo–N/C@MoS_2	Mo–N	ZIF-8	$Zn(NO_3)_2$	2-methylimidazole	$[(NH_4)_6Mo_7O_{24} \cdot 4H_2O]$, $SC(NH_2)_2$	ZIF-8, N/C@MoS_2	ZIF-8 (800 °C, 5 °C·min^{-1}, N_2, 2 h); N/C@MoS_2 (800 °C, 5 °C·min^{-1}, Ar, 2 h)	[93]

Table 6 Summary of ORR electrocatalytic activities of MOF-based non-noble metal (Cu, Mn, Ni, Mo) catalysts

Catalyst	Metal content	Hetero- atom content	I_D/I_G	S_{BET}/ ($m^2 \cdot g^{-1}$)	Catalyst loading/ ($m^2 \cdot g^{-1}$)	Electrolyte ($0.1\ mol \cdot L^{-1}$)	E_{onset}/V(vs. RHE)	$E_{1/2}$/V(vs. RHE)	Tafel slope/ ($mV \cdot dec^{-1}$)	n	H_2O_2 yield/%	Refs.
Cu_3P@NPPC-650	–	–	1.150	1004.7	0.200	KOH	–	0.780	–	3.96–4.00	8.00	[84]
CuNC/KB-400	0.28 at% Cu	1.59 at%N, 1.38 at% O	–	394.3	0.243	KOH	–	0.820	–	3.92–3.94	3.70	[85]
Cu–N/C	0.69 wt% Cu	1.21 at% N	1.060	–	0.380	KOH	1.029	0.813	81.0	3.80	–	[86]
25% Cu–N/C	5.51 wt% Cu	11.04 at% N	–	1182.0	0.250	KOH	0.914	0.813	45.8	3.94	5.20	[87]
Ni@NiNC-600	3.17 at% Ni	11.45 at% N	1.010	374.0	0.360	KOH	0.880	0.850	64.0	–	3.00	[88]
Ni-NSPC-6	2.30 at% Ni	10.60 at% N, 4.80 at% S	–	111.6	0.800	KOH	0.080 (vs. Ag/AgCl)	–	66.0	3.70	14.65	[89]
Ni-GT-750-A	–	–	1.110	428.5	0.250	KOH	0.910	–	60.0	4.00	–	[90]
MnO@NC-1100	5.45 wt% Mn	–	1.380	123.9	–	KOH	0.900	0.740	88.5	4.00	–	[91]
Mn_3O_4@NCP	–	–	1.192	613.0	0.400	KOH	0.920	0.8080	–	3.91–4.00	3.00	[92]
Mo–N/C@MoS_2	–	17.7 at% N	1.010	519.5	–	KOH	0.900	0.810	–	3.96	–	[93]

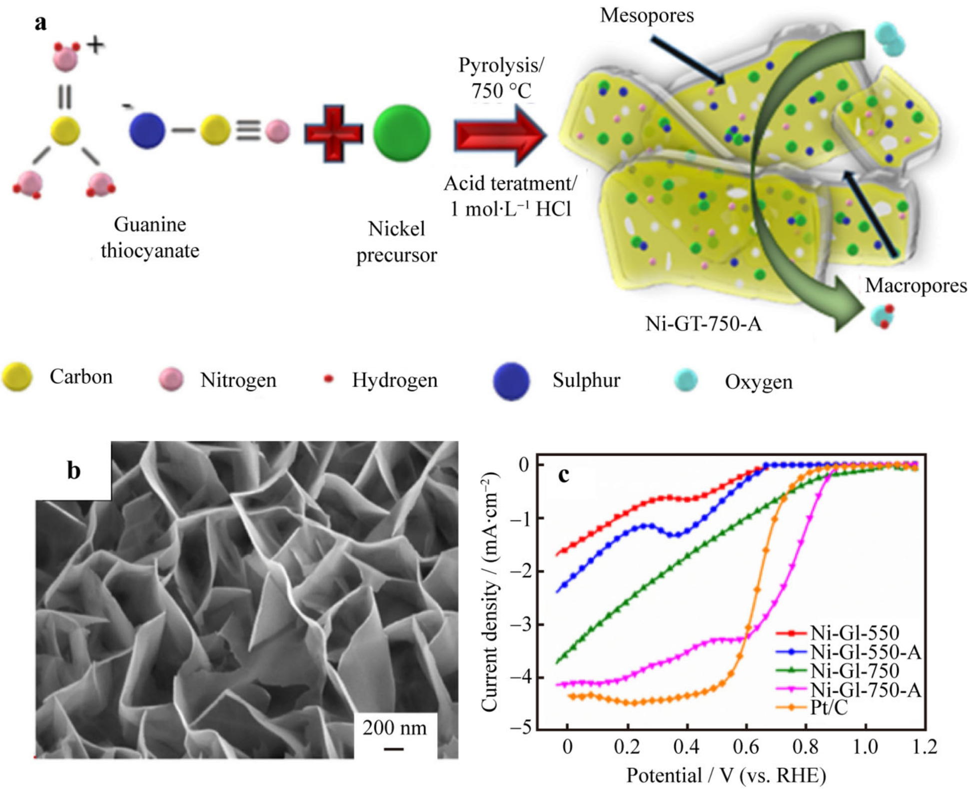

Fig. 10 **a** Pictorial scheme for illustration of synthesis procedure of Ni-GT-750-A; **b** HAADF-STEM image of Ni-GT-750-A; **c** LSV curves of Ni-GT-750-A in 0.1 mol·L^{-1} KOH (aq.). Reproduced with permission from Ref. [90]. Copyright 2020 Elsevier Inc.

pyrolysis. The pyrolysis conditions were in a N_2 atmosphere at 800 °C for 2 h. After adding 0, 2, 4, 6 and 8 mmol PVP, the specific surface area of the prepared P-ZIF catalyst was firstly increased and then decreased. When the dosage of PVP was 4 mmol, the maximum specific surface area was 548 m^2·g^{-1}. In addition to a higher specific surface area, P-Co-NC-4 catalyst had a higher N content (1.88 at%), which was conducive to combining with Co atoms embedded in C to form Co–N_x active sites and enhance the catalytic activity. It also showed an onset potential of 0.90 V (vs. RHE), a half-wave potential of 0.85 V (vs. RHE), and a 4-electron mechanism. Guan et al. [73] synthesized a single-hole cobalt/N-doped carbon hollow particle, which was mainly based on PVP modified PS sphere as template, and then a MOF (ZIF-67) shell was grown on the surface of the PS sphere. During the pyrolysis process, PS spheres were decomposed into hydrocarbon gas, which escaped from the interior and formed holes on the surface of the carbon shell. The size of surface pores was related to the heating rate. Especially when the heating rate was 10 °C·min^{-1}, strong gas emissions would completely destroy the hollow spheres. When the heating rate was 5 °C·min^{-1}, single-hole hollow spheres were formed. The hollow spheres with large holes not only helped to make full use of the internal catalytic sites, but also promoted the transport of electrolyte and the formation and release of catalytic products. The single-hole Co–N–C hollow particle catalyst exhibited an onset potential of 0.98 V (vs. RHE), a half-wave potential of 0.87 V (vs. RHE), and a Tafel slope of 102 mV·dec^{-1}. Moreover, after continuous operation for 24 h, the catalyst retained 92% of the original current, while the Pt/C catalyst lost about 36.5% after 16 h, indicating good stability. Chen et al. [74] synthesized hollow porous carbon spheres co-doped with ultra-small Co NPs by pyrolyzing a core–shell precursor composed of PS core and bimetallic Zn-Co-ZIFs (BMZIFs) shell (Fig. 7 [74]). The Zn ions in BMZIFs could not only spatially separate Co species to prevent Co NPs from aggregating, but also evaporate during pyrolysis to provide additional pores, and the PS core would decompose to create a unique hollow structure as well. Owing to the large surface area (737.4 m^2·g^{-1}), high porosity (pore volume = 0.81 cm^3·g^{-1}), tunable particle size (d = 4.28 nm), high graphitization degree (I_D/I_G = 0.95), and rich in highly active Co–N_x sites, the Co-HNCS-0.2 catalyst exhibited a remarkable ORR activity with the onset and half-wave potentials of 0.94 V (vs. RHE), and 0.82 V (vs. RHE), respectively, which was higher than that of commercial 20% Pt/C catalyst (0.93 V (vs. RHE) and 0.80 V (vs. RHE), respectively).

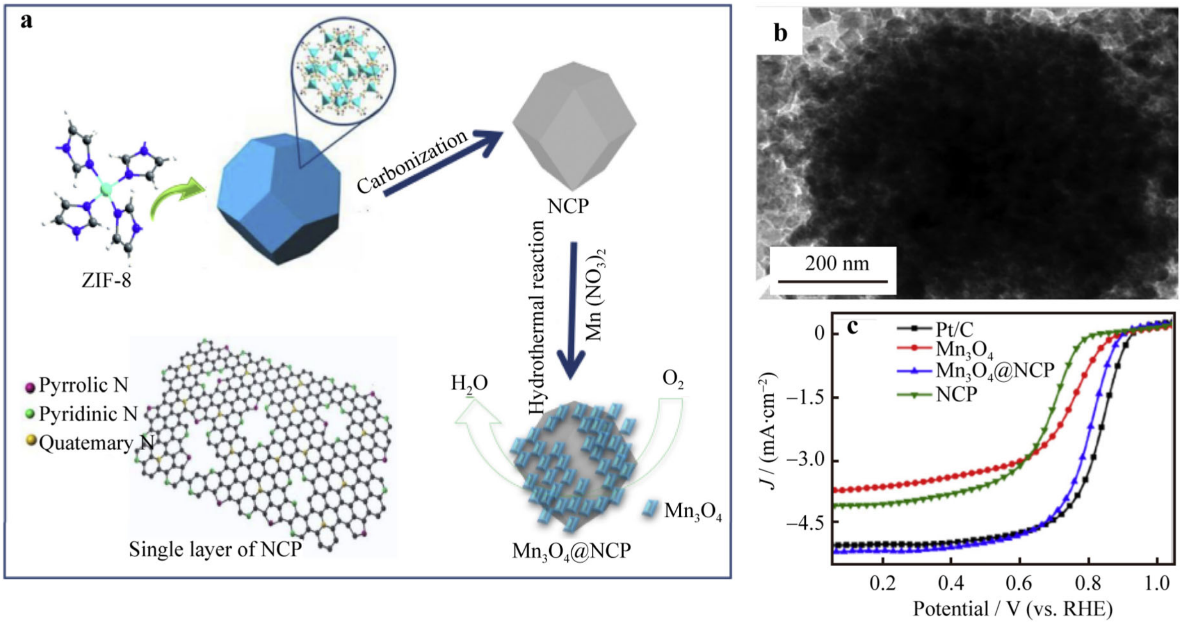

Fig. 11 **a** Graphical expression of synthetic method; **b** TEM image of Mn_3O_4@NCP; **c** LSV curves of Mn_3O_4@NCP in 0.1 mol·L^{-1} KOH solution. Reproduced with permission from Ref. [92]. Copyright 2020 Elsevier Ltd.

Owing to the outstanding conductivity and processability, graphene occupies an important position in the field of material composites and catalysis [81, 82]. In the preparation of cobalt oxide, in addition to using oxygen or air for oxidation, graphene oxide (GO) can also be used as an oxygen source, as it has rich oxygen-containing groups that can improve the conductivity of the catalyst. For example, Cai et al. [75] mixed GO and 2-methylimidazole, and then added Co^{2+} to self-assemble Co-MOF layer by layer on the GO surface. As a substrate, GO was negatively charged in water, while 2-methylimidazole was positively charged in water, and they were held together by electrostatic attraction. The subsequent addition of Co^{2+} would coordinate with 2-methylimidazole to form Co-MOF on the GO surface. Different layers of Co-MOF/GO were obtained by repeated impregnation. After pyrolysis in a N_2 atmosphere at 600 °C for 5 h, the Co-MOF was converted into a Co/N-doped porous carbon catalyst with BET specific surface area of 252 m^2·g^{-1} and I_D/I_G ratio of 0.99, providing porous channels and high active sites for the catalyst. Co–N_x and CoO_x can be used as catalytic active centers to improve electrocatalytic performance. GO can be reduced to graphene (rGO), thus effectively improving the conductivity of the catalyst and preventing the aggregation of MOF precursors with metal particles. In 0.1 mol·L^{-1} KOH (aq.), the Co–N–C/rGO-6-600 catalyst exhibited an onset potential of 0.963 V (vs. RHE), a half-wave potential of 0.87 V (vs. RHE), a Tafel slope of 54 mV·dec^{-1}, and a 4-electron mechanism. The stability test showed that the current of CO–N–C/RGO-6-600 maintained 97% under the long-term operation of 10,000 s, while the current loss of Pt/C catalyst was 7%. Guo et al. [76] used thermally shock exfoliated GO (EGO) as a substrate to grow modified ZIF-67 crystals in situ [83], and prepared Co_3O_4/Co@N-G-450 as an ORR catalyst. EGO had a high specific surface area (∼ 700 m^2·g^{-1}) and a soft porous network (∼ 2 to 200 nm in size). The surface contained a large number of oxygen functional groups and defects, which was conducive to the anchoring and growth of ZIF-67. During the synthesis process, it was very important to control the concentration of precursors, since ZIF overgrowth could lead to particle aggregation and dissociation. In addition, the control of pyrolysis temperature was also very important, because the oxygen functional groups of EGO would dissociate at high temperature, leading to the etching of ZIF-67 and the oxidation of Co center. When ZIF was loaded with 60 wt%, the pyrolysis yield was as high as 65% after pyrolysis in N_2 at 450 °C for 6 h. The Co_3O_4/Co@N-G-450 catalyst exhibited an onset potential of 0.962 V (vs. RHE), a half-wave potential of 0.808 V (vs. RHE), and a Tafel slope of 62 mV·dec^{-1}. Long-term stability test showed that after continuous operation for 50 h, the Co_3O_4/Co@N-G-450 catalyst remained 75% activity. Additionally, it was found by Yi et al. [77] that carbon black (CB) could not only improve the conductivity of Co-MOF, but also regulate the N type. The Co-MOF was prepared with 3,5-dimethyl-4-carboxypyrazole and Co^{2+}, and then the mixture of MOF and CB was pyrolyzed to prepare Co–Co_xO/N-doped carbon catalyst. The results revealed that when the mass ratio of MOF to CB was 3:1,

Table 7 Summary of synthesis of MOF-based non-noble multi-metallic catalyst

Sample	Active site	Multi-metal MOF			Lord	Pyrolysis precursor	Pyrolysis conditions	Refs.
		Type	Central ion	Ligand				
FeCo-NC	Fe–N, Co–N	Co/Zn ZIF	$Co(NO_3)_2$, $Zn(NO_3)_2$,	2-methylimidazole	$Fe(acac)_3$	Fe–Co/Zn ZIF	900 °C (5 $°C·min^{-1}$, N_2, 3 h)	[109]
FCPA-900	P-O-TM	Fe/Co-MOF	$FeCl_3$, $CoCl_2$	Phytic acid	–	Fe/Co-MOF	900 °C (Ar, 3 h)	[110]
Fe_3Mn_1/NCNTs-100	Fe–N_x	MOF-74	$MnCl_2$, $Fe(NO_3)_3$	2,5-dihydroxylbenzoic acid	Melamine	MOF-74 + melamine	800 °C (5 $°C·min^{-1}$, N_2, 2 h)	[111]
Ce-HPCN	CeO_2, Co–N_x	Ce-ZIF-L	$Zn(NO_3)_2$, $Co(NO_3)_2$, $Ce_2(OH)_4SO_4$	2-methylimidazole	–	Ce-ZIF-L	850 °C (2 $°C·min^{-1}$, Ar, 2 h)	[112]
CoPNi-N/C	Co–Ni alloy, Co/Ni atoms	CoPNi-MOF	$Co(NO_3)_2$, tris-1,10-phenanthroline nickel(II) nitrate	2-methylimidazole	–	CoPNi-MOF	750 °C (N_2, 3 h)	[113]

Table 8 Summary of ORR electrocatalytic activities of MOF-based non-noble multi-metallic catalyst

Catalyst	Metal content	Hetero$^-$ atom content	I_D/I_G	S_{BET}/($m^2·g^{-1}$)	Catalyst loading/($m^2·g^{-1}$)	Electrolyte (0.1 $mol·L^{-1}$)	E_{onset}/V(vs. RHE)	$E_{1/2}$/V(vs. RHE)	Tafel slope/($mV·dec^{-1}$)	n	H_2O_2 yield/%	Refs.
FeCo-NC	0.31 at% Co, 0.54 at% Fe	2.94 at% N	0.91	647.6	0.127	KOH	–	0.855	–	3.90	4.0	[109]
FCPA-900	0.16 wt% Fe, 1.20 wt% Co	0.90 wt% P	–	1646.0	0.408	KOH	0.91	0.840	78	3.91–3.98	–	[110]
Fe_3Mn_1/NCNTs-100	0.54 at% Fe, 0.34 at% Mn	4.34 at% N	1.00	104.2	0.100	NaOH	–	0.865	–	3.95	–	[111]
Ce-HPCN	–	–	–	501.2	0.1600	KOH	–	0.831	91	3.87	5.6	[112]
CoPNi-N/C	1.50 wt% Co, 0.22 wt% Ni	10.29 wt% N	1.03	446.8	0.300	KOH	0.93	0.840	43	3.90	–	[113]
						$HClO_4$	0.86	0.730	61	3.60	–	

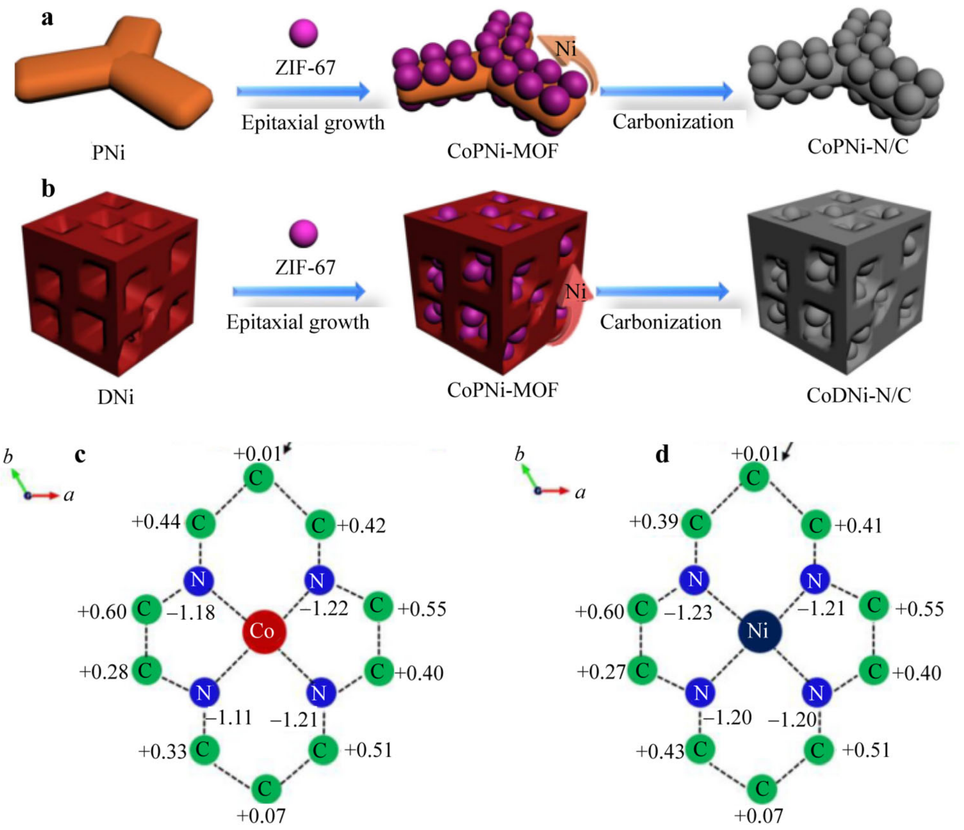

Fig. 12 Schematic illustration of synthesis process for **a** CoPNi-N/C and **b** CoDNi-N/C; plane averaged electron density difference of **c** Co–N/C and **d** CoXNi-N/C models. Reproduced with permission from Ref. [113]. Copyright 2019 Elsevier B.V.

CB effectively increased the total content of pyridinic-N and graphitic-N. It accounted for more than half of the total N and showed the best ORR catalytic activity. Moreover, CB could not only effectively increase the conductivity of the catalyst and promote electron transfer, but also improve the dispersibility of Co NPs, thus enhancing the catalytic activity. The BET specific surface area of MOF(Co)/CB (3:1)-500 catalyst was 203.5 $m^2 \cdot g^{-1}$. It also had an onset potential of 0.92 V (vs. RHE), a half-wave potential of 0.8 V (vs. RHE), and a Tafel slope of 51 $mV \cdot dec^{-1}$. The measured electron transfer number was 3.91–3.98 (0.06 to 0.56 V (vs. RHE)), suggesting a favorable ORR catalyst.

3.4 Preparation of Co-based catalyst by carbonization of Co-loaded MOF

In addition to being a pyrolysis precursor for catalysts, MOF can also be used as a synthesis template to provide a favorable structure. For example, Park et al. [78] designed a mixed MOF (ZIF-L@ZIF-67) with leaf core–shell structure as the precursor to prepare porous carbon leaves Co, N-PCLs catalyst after pyrolysis (Fig. 8 [78]). ZIF-L was synthesized hydrothermally with Zn^{2+} and 2-methylimidazole as the core, and then a ZIF-67 layer made of Co^{2+} and 2-methylimidazole was grown on the core surface as the shell. After 5 h pyrolysis in N_2 atmosphere at 800 °C, the Co, N-PCLs catalyst was produced, which maintained the original form of ZIF-L and formed more CNTs on the surface. Compared with C-ZIF-L (38 $m^2 \cdot g^{-1}$ and 0.03 $cm^3 \cdot g^{-1}$) and C-ZIF-67 (254 $m^2 \cdot g^{-1}$ and 0.18 $cm^3 \cdot g^{-1}$), the Co, N-PCLs catalyst had higher specific surface area (319 $m^2 \cdot g^{-1}$) and porosity (0.22 $cm^3 \cdot g^{-1}$), which were conducive to electrolyte penetration and electron transfer. Besides, it showed an onset potential of 0.992 V (vs. RHE), a half-wave potential of 0.91 V (vs. RHE), and a diffusion limiting current density of 5.22 $mA \cdot cm^{-2}$, which was similar to Pt/C catalyst but higher than C-ZF-L ($E_{1/2} = 0.592$ V (vs. RHE), $J_L = 1.86$ $mA \cdot cm^{-2}$) and C-ZF-67 ($E_{1/2} = 0.831$ V (vs. RHE), $J_L = 3.56$ $mA \cdot cm^{-2}$). Meanwhile, the electrochemical stability of the Co, N-PCLs catalyst was higher than that of Pt/C. Bhattacharyya et al. [79] prepared NCD-1, a N-doped carbon dot, through hydrothermal synthesis of anionic Mg-MOF, composite pyrolysis of NCD-1, and 5,10,15,20-tetrakis (4-methoxyphenyl)-21H,23H-porphine cobalt (II) as a cobalt source. In 0.1 $mol \cdot L^{-1}$ KOH (aq.), the onset potential of Co@CN catalyst was 0.8 V (vs. RHE), which was higher than that of NCD-1 catalyst

(0.36 V (vs. RHE)), and the yield of H_2O_2 was 4%, far lower than that of NCD-1 (40.8%). The loading of Co had a positive effect on improving the catalytic performance of N-doped C materials, because Co and N combined to form the active sites of Co–N_x, while cobalt oxide could promote the ORR catalytic reaction. Compared with the direct synthesis of Co-MOF, the selection of suitable supported Co catalyst for the preparation of Co-based catalyst is a little more complex, but can enhance the advantages of Co-supported catalyst.

3.5 Summary of cobalt-based catalyst

As a short conclusion, there are various synthesis strategies and methods for Co-MOF. According to the coordination number of Co ions and the coordination form of organic ligands, Co-MOF with different morphologies can be designed to further prepare high-performance ORR catalyst. Hybrid doping provides more possibilities for Co-based catalysts. The addition of heteroatoms can not only change the pyrolysis behavior of Co-MOF, increase the specific surface area, and adjust the pore size, but also enhance the activity of the catalyst. Whichever method is used to prepare the highly active co-catalyst, the following factors are worth considering: (1) Determine the active site of Co-based catalyst and take it as the starting point of the design materials; (2) Promote the formation of active sites, e.g., heteroatom doping and material composite; (3) High conductivity and porous network structure are conducive to electron transfer and reaction rate.

4 Other MOF-based non-noble metal (Cu, Mn, Ni, Mo) catalysts

4.1 Cu-based catalysts

In addition to Fe–N–C and Co–N–C catalysts with excellent performance, many non-noble metal catalysts with other metal ions are also worth for further exploration and development. Copper is an abundant and cost-effective metal on earth with high conductivity (close to silver), which can promote electron transfer and exhibit great potential in the ORR field. The research progress of Cu-based ORR catalysts in recent years was reported. Wang et al. [84] used N-containing pyrazine and P-containing 1-hydroxyethylidene-1,1-diphosphoonic acid as organic ligands, and then self-assembled with Cu^{2+} to prepare Cu–NPMOF by in situ doping of N and P (Fig. 9 [84]). The reasonable selection of MOF with multiple heteroatoms (such as N, P, S) as single-source precursor is a good strategy to obtain catalyst with uniform doping, higher component repeatability, high activity and stability. Cu–NPMOF was pyrolyzed at 650 °C in a N_2 atmosphere to prepare Cu@NPPC (Table 5 [84–93]). Then, it was ground and mixed with $NaH_2PO_2 \cdot H_2O$ for secondary pyrolysis (250 °C, N_2). Finally, the graded porous carbon-containing Cu_3P NPs (Cu_3P@NPPC-650 catalyst) was produced. The specific surface area of Cu_3P@NPPC-650 (1004.7 $m^2 \cdot g^{-1}$) was much higher than that of Cu@NPPC-650 (402.5 $m^2 \cdot g^{-1}$). This was because $NaH_2PO_2 \cdot H_2O$ could form pores during pyrolysis after decomposition. The porous carbon shells with high specific surface area, the active sites of Cu_3P NPs, and the heteroatoms doping were the main reasons for its high performance. In 0.1 $mol \cdot L^{-1}$ KOH (aq.), Cu_3P@NPPC-650 catalyst had a half-wave potential of 0.78 V (vs. RHE), only 29 mV lower than Pt/C catalyst (Table 6 [84–93]), and its stability was better than Pt/C catalyst. Li et al. [85] prepared Cu-MOF/KB by mixing Cu^{2+}, 1,4-benzenedicarboxylic, triethylenediamine and HNO_3-functionalized KB (Ketjenblack carbon, EC-300J). After pyrolysis at 800 °C, the final CuNC/KB-400 catalyst was yielded. Using Cu-MOF as template, KB was modified to obtain a novel hybrid catalyst which could form Cu/Cu_2O NPs and amorphous CuN_xC_y. The conductivity of CuNC/KB-400 was 5.62 $S \cdot cm^{-1}$ and the specific surface area was 394.3 $m^2 \cdot g^{-1}$. In CuNC/KB-400, Cu/Cu_2O NPs and CuN_xC_y could synergistically improve ORR performance, leading to higher half-wave potential (0.82 V (vs. RHE)) and diffusion limiting current density (6.05 $mA \cdot cm^{-2}$) than Pt/C catalyst.

Obviously, doping Cu^{2+} into MOF precursor is a common strategy to prepare Cu-based catalyst. Xie et al. [86] used adsorption method to combine Cu^{2+} to ZIF-8 framework, and after further pyrolysis at 1000 °C to produce Cu–N/C catalyst with Cu NPs and Cu(II)-N active sites (the Cu content was 0.69 wt%). Although Cu doping would make the total N content (1.21 at%) and pyridinic-N content (0.18 at%) in Cu–N/C lower than that in N/C (3.80 at% and 1.08 at%, respectively), the ORR activity of Cu–N/C catalyst was much higher than that of N/C catalyst. The half-wave potential of Cu–N/C was 0.813 V (vs. RHE), similar to Pt/C (0.821 V (vs. RHE)), but higher than that of N/C (0.775 V (vs. RHE)). Furthermore, compared with Pt/C (84 $mV \cdot dec^{-1}$) and N/C (120 $mV \cdot dec^{-1}$), the Tafel slope of Cu–N/C was lower (81 $mV \cdot dec^{-1}$), indicating that the presence of Cu species could effectively improve the ORR kinetic of N-doped carbon. After treating Cu in Cu–N/C with 1 $mol \cdot L^{-1}$ HNO_3, it was found that the half-wave potential reduced from 0.813 to 0.764 V (vs. RHE), and J_L decreased from 6.0 to 4.38 $mA \cdot cm^{-2}$. This result showed that Cu (0) NPs could stabilize the adjacent Cu(II)–N (i.e., N–Cu(II)–Cu(0)). Lai et al. [87] also prepared Cu-ZIF-8 by adsorption method, and then obtained Cu–N/C catalyst through pyrolysis at 900 °C under N_2 atmosphere. By controlling the copper load and effectively regulating the states of Cu (II) and Cu (0), the highly active hybrid coordination sites of N–Cu(II)–Cu(0) were constructed. For the 0%, 25% and 40% Cu–N/C samples, the Cu content was 2.96 wt%, 5.51 wt% and 9.90 wt%, as well the N content was 11.20 wt%, 11.04 wt% and 9.05 wt%, respectively. For the 40% Cu–N/C sample with high Cu doping content, after pyrolysis, Cu in Cu-ZIF-8 was easier to form Cu NPs than Cu–N sites. On the contrary, when Cu–N/C content was 10%, Cu was mainly distributed in carbon matrix in the form of atomic size. Therefore, Cu content played an important role in the formation of Cu–N sites, and adjacent metallic Cu NPs would stabilize the Cu–N sites. The 25% Cu–N/C catalyst showed the best ORR activity. Its onset potential (0.914 V (vs. RHE)), half-wave potential (0.813 V (vs. RHE)), and J_L (5.50 mA·cm^{-2}) were very close to 30 wt% Pt/C (0.936 V (vs. RHE), 0.810 V (vs. RHE), 5.46 mA·cm^{-2}, respectively). Through the current time test, the current attenuation of 25% Cu–N/C was only 12.6% after continuous 10,000 s operation, while that of 30 wt% Pt/C described by 21.9%.

Generally, Cu–N/C is prepared by the pyrolysis of Cu-doped ZIF (without considering the pyrolysis atmosphere), and the Cu species can exist in the following states: (i) Cu (0) NPs; (ii) CuO_x; (iii) Cu–N_x (including Cu^+–N_2 and Cu^{2+}–N_4). Li et al. [94] etched Cu–N/C with 0.5 mol·L^{-1} H_2SO_4 and 1.3 mol·L^{-1} HNO_3, respectively, and obtained Cu–N/C-H_2SO_4 catalyst containing Cu^+–N_2, and Cu–N/C-HNO_3 catalyst containing Cu^{2+}–N_4. Then, the effects of Cu^+–N_2 and Cu^{2+}–N_4 on ORR process were discussed. Cu–N/C was prepared by pyrolysis of Cu-ZIF-L at 800 °C in N_2 atmosphere. The low concentration of H_2SO_4 removed the remaining zinc and possible metal oxides, and had little effect on the Cu–N structure. However, HNO_3 could not only remove metals and metal oxides, but also oxidize Cu^+ to Cu^{2+}. X-ray absorption near-edge structure (XANES) and extended X-ray absorption fine structure (EXAFS) spectra confirmed the presence of Cu^+–N_2 active sites in Cu–N/C-H_2SO_4, and Cu^{2+}–N_4 active sites in Cu–N/C-HNO_3. For Cu–N/C-H_2SO_4 and Cu–N/C-HNO_3, the Cu contents were 23.9 wt% and 7.9 wt%, respectively, and the specific surface areas were 774.3 and 895.3 m^2·g^{-1}, respectively. The E_{onset} (0.987 V (vs. RHE)) and $E_{1/2}$ (0.860 V (vs. RHE)) of Cu–N/C-H_2SO_4 catalyst were significantly higher than those of Cu–N/C-HNO_3 catalyst ($E_{\text{onset}} = 0.927$ V (vs. RHE), $E_{1/2} = 0.802$ V (vs. RHE)) and Cu–N/C catalyst ($E_{\text{onset}} = 0.985$ V (vs. RHE), $E_{1/2} = 0.800$ V (vs. RHE)). After 5000 cyclic voltammetry (CV) cycling test, the ORR activity of Cu–N/C-H_2SO_4 catalyst showed no obvious change, while the $E_{1/2}$ of Cu–N/C-HNO_3 and Pt/C catalyst displayed negative shift of 11 and 20 mV, respectively, indicating that Cu–N/C-H_2SO_4 had good catalytic stability. Li et al. [95] calculated the adsorption energy for O_2 and OOH at the Cu–N_2 and Cu–N_4 sites. The former had much higher O_2 and OOH adsorption energies, and the O–O bond stretching of O_2 and OOH was more prone to break (O–O bond length were 0.01455 and 0.01460 nm, respectively). Cu–N_4 showed relatively low adsorption energies for O_2 and OOH, 0.74 and − 0.23 V, respectively. The O–O bonds of O_2 and OOH were less stretched, at 0.01289 and 0.01435 nm, respectively. The higher adsorption energies of active sites and O–O stretching degree were helpful to promote the ORR process, which implied that Cu–N_2 had strong catalytic activity. For the preparation of Cu-based catalysts, it is noteworthy that the content and form of copper may maintain the predominance of precursor structures and the formation of active sites.

4.2 Other M-based catalysts (M = Ni, Mn, Mo)

Ni-based catalysts are often studied in the field of catalysis, but their catalytic performance in ORR is always inferior to that of Fe–N–C and Co–N–C catalysts [96–98]. Wang et al. [99] prepared electrocatalyst by self-assembly using metal ions (Fe, Co, Ni) and glycerin. The products were Fe_3C-CNTFs (210.610 cm^2·g^{-1}, 1.92 nm), Co-CNTFs (268.739 cm^2·g^{-1}, 2.21 nm) and Ni-CNTFs (284.416 cm^2·g^{-1}, 2.30 nm), which had similar specific surface area and average pore size. The electrocatalytic activity was in descending order: Co-CNTFs > Fe_3C-CNTFs > Ni-CNTFs. Their electron transfer numbers were 3.9, 2.9 and 2.7, respectively. Ni-CNTFS mainly covered the crystal surfaces of Ni (111) and Ni (200). By DFT calculation, Ni (111) had a strong binding energy (− 0.149 eV·atom^{-1}) to OOH, leading to a 2-electron dominated ORR process. However, Co (111)–OOH and Fe_3C (031)–OOH were unstable and prone to produce free OH^-, so they proceeded through the 4-electron reaction pathway. In addition, Zhao et al. [88] prepared the self-assembled Ni-FA from Ni^{2+} and folic acid in the presence of hydrazine. After pyrolysis at 600 °C, Ni-FA was converted into Ni@NiNC-600 catalyst with high N content (N: 11.45 at%). Echinops-like Ni@NiNC-600 contained a large number of regularly dispersed CNTs with a diameter of ~ 200 nm, and Ni NPs were enclosed in graphite shells composed of CNTs. Higher N content in Ni@NiNC-600 contributed to the formation of more Ni–N active sites, while CNTs could promote the conductivity. Owing to the synergistic effect of unique hierarchical porous nanostructure composed of numerous CNTs, Ni@NiNC was fixed on the microsphere, exposing abundant Ni–N active sites, and showing superior ORR performance in alkaline media. The catalyst's onset potential and half-wave potential ($E_{\text{onset}} = 0.88$ V (vs. RHE), $E_{1/2} = 0.85$ V (vs. RHE)) were higher than Ni@NiNC-350 ($E_{\text{onset}} = 0.59$ V (vs. RHE), $E_{1/2}$ = 0.65 V (vs. RHE)) and commercial Pt/C (E_{onset} = 0.86 V (vs. RHE), $E_{1/2}$ = 0.84 V (vs. RHE)).

The addition of heteroatoms can effectively improve the electrocatalytic performance of Ni-based catalysts. For example, Yan et al. [89] reported a N, S double-doped rod catalyst (Ni-NSPC-6) prepared from nickel acetate and 2-mercapto-5-methyl-1,3,4-thiadiazole. After removing Ni and excess nickel sulfide with 6 mol·L^{-1} HCl, the remaining Ni_3S_2 NPs (520 nm) were wrapped in the amorphous carbon layer, preventing the dissolution and aggregation in the catalytic process. As the co-doping of N, S played a positive synergistic effect, the one-dimensional structure facilitated the electrode–electrolyte contact and promoted the transport of ions and electrons. The onset potential of Ni-NSPC-6 catalyst was 0.08 V (vs. Ag/AgCl), and its stability was better than that of Pt/C catalyst. Tyagi et al. [90] synthesized Ni-GT precursor using nickel nitrate hexahydrate and guanidine thiocyanate containing N and S, and then heated the precursor and treated it with acid to produce Ni-GT-750-A (Fig. 10 [90]). When the guanidine thiocyanate was decomposed at high temperature (~ 1000 °C), Ni might bond with sulfur to form Ni_xS_y (NiS and Ni_3S_2). The Ni/Ni_xS_y NPs and N, S-doped carbon substrates had good dispersion, which jointly promoted the ORR, so the NI-GT-750-A catalyst exhibited positive onset potential in acidic and alkali electrolytes (0.89 V (vs. RHE), and 0.91 V (vs. RHE), respectively). Therefore, through the reasonable design and preparation, Ni-based catalyst can also have good ORR performance.

Manganese oxide (MnO_x) is a common non-noble metal catalyst and can be applied into the fields of OER and ORR [100–102]. Through effective means, MnO_x can be designed into various forms (such as nanocrystalline particles, nanorods and nanotubes); however, the ORR activities of MnO_x in different valences, and crystal structures are different [103]. Furthermore, the weak conductivity of MnO_x greatly limits its development. Combined with large scale, high porosity and high conductivity, the catalytic performance of MnO_x can be promoted. For instance, Ji et al. [91] synthesized a bimetallic N-rich tetrazolate-based MOF (Cd/Mn-MOF) and used it as a precursor to prepare the MnO@NC-1100 catalyst by pyrolysis at 1100 °C. During the pyrolysis process, Cd (II) evaporated (the boiling point is 765 °C), and tetrazolate would explode, leading to the formation of pores. After thermal annealing, MnO@NC-1100 was mainly composed of carbon nanorods and a small amount of MnO particles wrapped in graphene-like carbon layers. The MnO@NC-1100 catalyst showed significant ORR activity in 0.1 mol·L^{-1} KOH (E_{onset} = 0.90 V (vs. RHE), $E_{1/2}$ = 0.74 V (vs. RHE)), and its activity did not decrease greatly after 2000 cycles. Najam et al. [92] took the N-doped carbon polyhedrons (NCP) prepared by the pyrolysis of ZIF-8 as template, and then hydrothermally reacted with $Mn(NO_3)_2$ to obtain Mn_3O_4@NCP catalyst, which contained the oriented growth of Mn_3O_4 nanotubes and porous NCP (Fig. 11 [92]). Although the specific surface area of Mn_3O_4@NCP (613 m^2·g^{-1}) was only half that of NCP (1364 m^2·g^{-1}), it had very high pyridinic-N (34.51 at%) and graphitic-N (30.76 at%) content. The presence of Mn may be responsible for nitrogen protection. The mesoporous carbon structure with high N content (pyridinic-N and graphitic-N) reduced the adsorption energy barrier of O_2 and improved the ORR performance. The Mn_3O_4@NCP catalyst and Pt/C catalyst had the same E_{onset} (0.92 V (vs. RHE)) and similar diffusion limiting current density (5.24 and 5.0 mA·cm^{-2}, respectively). The H_2O_2 yield of Mn_3O_4@NCP was less than 3%, lower than that of Pt/C (5%) and NCP (30%), indicating that it was an excellent ORR catalyst.

Recently, 2D metal sulfide material, MoS_2, has attracted wide attention in the field of electrocatalysis with excellent electrical and optical properties [104–107]. Amiinu et al. [93] prepared N-doped porous carbon matrix (N/C) by the pyrolysis of ZIF-8, and then the MoS_2 nanosheets were in situ generated on the N/C. After heat treatment at 800 °C, Mo–N/C@MoS_2 catalyst was obtained. The semiconductor properties of MoS_2 and the formation of Mo–N sites were beneficial to improve the catalytic activity of Mo–N/C@MoS_2. It presented similar onset and half-wave potential (E_{onset} = 0.90 V (vs. RHE), $E_{1/2}$ = 0.81 V (vs. RHE)) with Pt/C catalyst (E_{onset} = 0.92 V (vs. RHE), $E_{1/2}$ = 0.81 V (vs. RHE)). Mo–N/C@MoS_2 displayed larger diffusion limiting current density ($J_L = -5.3$ mA·cm^{-2}) than Pt/C ($J_L = -4.9$ mA·cm^{-2}). The ORR activity of Mo–N/C@MoS_2 catalyst mainly came from the synergistic effect of Mo–N and N/C phase, especially the combination of N doping and high concentration of pyridine-N, which enhanced the adsorption and reduction of oxygen. So far, there have been few studies on the preparation of M-based catalysts (M = Ni, Mn, Mo) using MOF as the precursor. Admittedly, the ORR performance of these non-noble metals is similar to that of Pt/C when properly designed and prepared, and the unique advantages of different metal centers suggest that there is still much room for improvement.

5 MOF-based non-noble multi-metal catalyst

Compared to single-metal catalysts, multi-metal composites are used to improve the ORR performance of catalysts, because the multi-metal components usually exhibit synergistic effects to improve the ORR performance. Multi-metal MOF is an excellent precursor for the synthesis of multicomponent non-noble metal catalysts, especially Fe or Co-centered metal MOF with catalytic potential [108]. For example, Wu et al. [109] utilized Co/Zn-ZIF with unique porous structure as a cage to capture Fe(III) to synthesize FeCo-NCs catalyst by pyrolysis at 600 °C (Table 7 [109–113]). Fe and Co can be well dispersed in the carbon matrix and form Fe–N and Co–N active sites with N atoms, thereby synergistically promoting electrocatalytic performance. The FeCo-NC catalyst had a high specific surface area of 647.6 $m^2 \cdot g^{-1}$ and lamellar pores, showing an activity ($E_{1/2}$ = 0.855 V (vs. RHE)) comparable to Pt/C ($E_{1/2}$ = 0.827 V (vs. RHE)) (Table 8 [109–113]). Moreover, Wang et al. [110] incorporated the synthesized Fe and Co into P-doped porous carbon catalyst (FCPA-900), which was derived from Fe/Co-MOF precursor by in situ carbonization. The specific surface area of the sample after carbonization at 900 °C was relatively high (1646 $m^2 \cdot g^{-1}$), which was conducive to the transportation of reactants. Since P doping changed the symmetry of the spin density of carbon atom, and the P–O–Fe or P–O–Co bond changed the electronic structure, the catalyst showed excellent ORR performance and stability.

In addition to Fe and Co bimetallic catalyst, Fe or Co with other non-noble multi-metallic catalysts are also promising for ORR activity. Dong et al. [111] prepared Fe_3Mn_1/NCNTs-100 catalyst by synthesizing MOF-74 (Fe and Mn as the metal ions) and adding melamine as the N source for pyrolysis. By adjusting the molar ratio of Fe and Mn, it was found that the addition of Fe could significantly reduce the particle size of the sample, and the presence of Mn ions and melamine could promote the formation of CNTs. By comparing the concentration of melamine, it was found that the higher the concentration, the larger the diameter of CNTs. Fe_3Mn_1/NCNTs-100 was a typical core–shell structure, containing a small amount of NPs (average diameter of ~ 26.0 nm) wrapped by CNTs (~ 80 nm in diameter). Owing to the unique microstructure of Fe–Mn alloy coated with multilayer N-doped CNTs, high pyridinic-N content (57.32%) and Fe–N_x active sites, Fe_3Mn_1/NCNTs-100 catalyst showed the best performance at the ORR activity with $E_{1/2}$ of 0.865 V (vs. RHE) and J_L of − 5.33 $mA \cdot cm^{-2}$, compared with commercial Pt/C catalyst (0.855 V (vs. RHE) and − 5.27 $mA \cdot cm^{-2}$). Besides, Xia et al. [112] synthesized a 2D-hexagonal-leaf-like ZIFs lamella (ZIF-L) precursor by solution-mediated method, and then pyrolyzed to prepare a novel Ceria@2D-hexagonal-leaf-like hierarchical porous carbon nanosheets (Ce-HPCN). Since N atoms in 2-methylimidazole tended to connect with H atoms in H_2O to form N–H–N, adding a small amount of aqueous solution could induce the conversion of Co-Zn-ZIF to 2D ZIF-L. Ce-HPCN showed good electrocatalytic performance ($E_{1/2}$ = 0.831 V (vs. RHE)), close to 30% Pt/C catalyst ($E_{1/2}$ = 0.846 V (vs. RHE)). The result was due to the synergistic effect of Co–N_x and CeO_2, especially the coexistence of Ce^{4+} and Ce^{3+} redox couple was conducive to O_2 adsorption. Moreover, Xu et al. [114] used $NiCl_2 \cdot 6H_2O$, $Co(NO_3)_2 \cdot 6H_2O$, 2-methylimidazole, and terephthalic acid as raw materials to prepare 2D multi-metallic MOF (Co, Ni MOF), and then further transferred to the Co, Ni-embedded N-doped porous carbon (CoNi-NC) catalyst with a high specific surface area of 362 $m^2 \cdot g^{-1}$ through pyrolysis at 900 °C for 2 h. The prepared bimetallic CoNi-NC retained the nanoleaf morphology and contained some graphitic nanotubes in the nanoleaf. The CoNi-NC catalyst exhibited high-efficiency ORR catalytic performance. Its onset potential was 1.038 V (vs. RHE), and the half-wave potential was 0.866 V (vs. RHE), which were higher than that of Pt/C catalyst (E_{onset} = 1.006 V (vs. RHE), $E_{1/2}$ = 0.850 V (vs. RHE)). Li et al. [113] prepared PNi-MOF and DNi-MOF with different morphologies by reaction of nickel nitrate with tris-1,10-phenanthroline and dimethylglyoxime (Fig. 12 [113]). Then, ZIF-67 was epitaxially grown on the surface of PNi-MOF and DNi-MOF. After pyrolysis at 750 °C for 3 h, a two-atom Co/Ni dual sites was obtained in N-doped porous carbon catalysts (CoPNi-N/C and CoDNi-N/C). The measured specific surface area for CoPNi-N/C was 446.8 $m^2 \cdot g^{-1}$, and 398.3 $m^2 \cdot g^{-1}$ for CoDNi-N/C. Their V_{mic}/V_t (the ratio of micropore volume to total pore volume) values were 41.72% and 27.06%, respectively, much higher than that of Co–N/C (354.9 $m^2 \cdot g^{-1}$ and 22.4%). It was worth noting that in the Co–N/C system, the two N atoms can obtain 1.18 and 1.11 electrons; while in the CoXNi–N/C (X = P or D) system, two N atoms can obtain 1.23 and 1.20 electrons, indicating that the Ni–N bond can increase the electron activity of N atoms. Under similar conductivity condition, the increase of electron concentration and hole concentration of the catalyst plays a more important role in the catalyst performance [115]. Therefore, compared with single metal Co–N/C catalyst, the addition of Ni can cause positive changes in the onset potential and reduction peak potential. The electrocatalytic activity analysis showed that the CoPNi-N/C catalyst was superior to CoDNi-N/C catalyst under both alkaline and acidic conditions. In 0.1 $mol \cdot L^{-1}$ KOH and 0.1 $mol \cdot L^{-1}$ $HClO_4$ aqueous solution, the CoPNi-N/C catalyst exhibited an onset potential of 0.93 V and 0.86 V (vs. RHE), a half-wave potential of 0.84 V (vs. RHE), and 0.73 V (vs. RHE), and a Tafel slope of 43 $mV \cdot dec^{-1}$ and 61 $mV \cdot dec^{-1}$, respectively. Meanwhile, the ORR activity of CoDNi-N/C catalyst was only slightly lower than that of CoPNi-N/C catalyst, because CoPNi-N/C had 41.72% micropores, higher than that of CoDNi-N/C, which was favorable for the absorption of oxygen molecules, thus reducing the ORR activation energy. The superior ORR activity made it the best electrocatalyst reported at that time. For the preparation of multicomponent catalysts with multi-metallic MOF, the selection and ratio of metals, as well as the existing form after pyrolysis, have an important effect on the performance of catalysts. The synergy between different metal phases can effectively improve the ORR activity, but the synergistic effect of non-noble multi-metal catalysts still need systematical study.

6 Summery and outlook

This review mainly summarized the preparation methods of non-noble metal ORR catalysts by MOF carbonization in recent three years from a synthesis perspective. Through the design of MOF precursor and carbonization conditions, the improvement of catalytic performance was discussed from the aspects of preparation, dispersion and exposure area of specific active sites, and the promotion strategy was proposed. In general, there are four different methods for synthesizing non-noble metal catalysts from MOF. (1) Direct pyrolysis of metal MOF using target metal-centered atoms is simple and effective. (2) MOF is used as the carrier to adsorb the target metal and then undergoes pyrolysis. Therefore, the choice of carrier and the doping amount of target metal have an important influence on the activity of catalyst. (3) The porous topological structure of MOF is used as template to synthesize the target product, and the morphology of the target product was optimized to increase the interface contact. (4) MOF is introduced in situ or mixed with heteroatom sources to further enhance the ORR catalytic activity. For most metal-based catalysts (M = Fe, Co, Cu, etc.), the main catalytic active centers are mainly M–N_x, which means that the pyrolysis precursor must have high N content and metal dispersibility. Similarly, the porosity, hydrophilicity and conductivity of carbon base also have important effects on the activity of the catalyst. These characteristics are mainly related to the precursor structure, pyrolysis conditions and post-treatment methods.

Designing the MOF structure at the molecular level is conducive to the dispersion of metals and heteroatoms, and the formation of effective active sites during pyrolysis. For non-noble metal ORR catalysts, in addition to the active sites of metal-N, the ratio and content of pyridinic-N, pyrrolic-N and graphitic-N also have a certain impact on the performance of catalysts. However, the type and content of N, and the formation of graphite carbon are mainly related to the pyrolysis temperature. Excessive pyrolysis temperature contributes to the formation of graphite carbon and specific surface area, but it will reduce the content of N and increase the diameter of the metal particles, which weaken the catalytic activity. Therefore, in the preparation of catalysts, it is indispensable to adjust the formulation ratio and pyrolysis temperature effectively to optimize the performance of catalysts. A good catalyst does not require a high metal content, but a relatively high nitrogen content, as this will facilitate the formation of the M–N_x site. At the same time, the structure of porous network is also an important part. However, larger specific surface area does not imply higher catalytic activity, which is related to the dispersion and exposure of active sites. This means that the active region of the catalyst can more intuitively characterize the activity of the catalyst than the specific surface area. Hence, in the design of MOF, the influence of multiple factors should be considered to determine the metal type and active site and make structure adjustments such as heteroatom doping, material composite, solution etching and pyrolysis condition, to prepare hydrophilic, conductive, porous and highly active catalysts.

Although many excellent non-noble metal ORR catalysts have been prepared by MOF carbonization, some problems still need to be solved. First of all, the preparation of non-noble metal catalysts by MOF carbonization is a better method, but how to shorten the synthesis cycle of catalysts and improve the pyrolysis yield is still a huge challenge. Secondly, studies on the preparation of non-noble metal catalysts by MOF pyrolysis mainly focus on iron, cobalt, nickel and copper, etc., while other non-noble metal ORR catalysts need further exploration. Thirdly, how to prepare catalysts with high activity, stability and corrosion resistance under acidic conditions is worth for further study. Fourthly, the synergistic effect of non-noble multi-metal catalysts should be studied systematically. Last but not least, it is undeniable that the doping of heteroatoms can improve the activity of catalysts. However, most of the studies on heteroatom doping focus on N and S, and few on P, B, F and other heteroatoms. It is worth discussing what role the heteroatoms play and in what ways.

Acknowledgements This study was financially supported by the National Natural Science Foundation of China (Nos. 21873027 and 21908046), Hubei Natural Science Foundation (No. 2019CFB293) and Ministry-of-Education Key Laboratory for the Synthesis and Application of Organic Functional Molecules (No. KLSAOFM1802).

References

[1] Yaghi OM, Li GM, Li HL. Selective binding and removal of guests in a microporous metal–organic framework. Nature. 1995;378(6558):703.

[2] Cheng WZ, Liang JL, Yin HB, Wang YJ, Yan WF, Zhang JN. Bifunctional iron-phtalocyanine metal–organic framework catalyst for ORR, OER and rechargeable zinc-air battery. Rare Met. 2020;39(7):815.

[3] Kang ZX, Fan LL, Sun DF. Recent advances and challenges of metal organic framework membranes for gas separation. J Mater Chem A. 2017;5(21):10073.

[4] Wu MX, Yang YW. Metal organic framework (MOF)-based drug/cargo delivery and cancer therapy. Adv Mater. 2017; 29(23):1606134.

[5] Zhou FL, Bao HF, Wu XS, Tao YL, Qin C, Su ZM, Kang ZH. High-performance metal–organic framework-based single ion conducting solid-state electrolytes for low-temperature lithium metal batteries. ACS Appl Mater Interfaces. 2019;11(46):43206.

[6] Li M, Song MY, Wu GT, Tang ZY, Sun YF, He YB, Li JH, Li L, Gu HS, Liu X, Ma C, Peng ZF, Ai ZQ, Lewis D. A free standing and self-healable 2D supramolecular material based on hydrogen bonding: a nanowire array with sub 2 nm resolution. Small. 2017;13(21):1604077.

[7] Qasem NAA, Ben-Mansour R, Habib MA. An efficient CO_2 adsorptive storage using MOF-5 and MOF-177. Appl Energy. 2018;210(15):317.

[8] Wang C, An B, Lin WB. Metal–organic frameworks in solid-gas phase catalysis. ACS Catal. 2019;9(1):130.

[9] Ferey G. A chromium terephthalate-based solid with unusually large pore volumes and surface area. Science. 2005;309(5743):2040.

[10] Park KS, Ni Z, Adrien P, Choi JY, Huang RD, Uribe-Romo FJ, Chae HK, O'Keeffe M, Yaghi OM. Exceptional chemical and thermal stability of zeolitic imidazolate frameworks. Proc Natl Acad Sci USA. 2006;103(27):10186.

[11] Yuan S, Feng L, Wang KC, Pang JD, Bosch M, Lollar C, Sun YJ, Qin JS, Yang XY, Zhang P, Wang Q, Zou LF, Zhang YM, Zhang LL, Fang Y, Li JL, Zhou HC. Stable metal organic frameworks: design, synthesis, and applications. Adv Mater. 2018;30(37):1704303.

[12] Sun L, Campbell MG, Dincă M. Electrically conductive porous metal–organic frameworks. Angew Chem Int Ed. 2016;55(11):3566.

[13] Miner E, Fukushima T, Sheberla D, Sun L, Surendranath Y, Dincã M. Electrochemical oxygen reduction catalysed by Ni_3(hexaiminotriphenylene)$_2$. Nat Commun. 2016;7(1):10942.

[14] Tripathy R, Samantara A, Behera JN. A cobalt metal–organic framework (Co-MOF): a bi-functional electro active material for the oxygen evolution and reduction reaction. Dalton Trans. 2019;48(28):10557.

[15] Fu SF, Zhu CZ, Song JH, Du D, Lin YH. Metal–organic framework-derived non-precious metal nanocatalysts for oxygen reduction reaction. Adv Energy Mater. 2017;7(19):1700363.

[16] Wen XD, Zhang QQ, Guan JQ. Applications of metal–organic framework-derived materials in fuel cells and metal-air batteries. Coord Chem Rev. 2020;409:213214.

[17] Qiao MF, Wang Y, Li L, Hu GZ, Zou GA, Mamat X, Dong YM, Hu X. Self-templated nitrogen-doped mesoporous carbon decorated with double transition-metal active sites for enhanced oxygen electrode catalysis. Rare Met. 2020;39(7):824.

[18] Gao LQ, Xiao ML, Jin Z, Liu CP, Ge JJ, Xing W. Hydrogen etching induced hierarchical meso/micro-pore structure with increased active density to boost ORR performance of Fe–N–C catalyst. J Energy Chem. 2019;35:17.

[19] Zhang C, Zhang W, Zheng WT. Transition metal-nitrogen-carbon active site for oxygen reduction electrocatalysis: beyond the fascinations of TM-N4. ChemCatChem. 2019;11(12):655.

[20] Wang Y, Li J, Wei ZD. Transition-metal-oxide-based catalysts for the oxygen reduction reaction. J Mater Chem A. 2018;6(18):8194.

[21] Liu YJ, Xie XL, Zhu GX, Mao Y, Ju SX, Shen XP, Pang H. Small sized Fe–Co sulfide nanoclusters anchored on carbon for oxygen evolution. J Mater Chem A. 2019;7(26):15851.

[22] Wang HF, Chen LY, Pang H, Kaskel S, Xu Q. MOF-derived electrocatalysts for oxygen reduction, oxygen evolution and hydrogen evolution reactions. Chem Soc Rev. 2020;49(5):1414.

[23] Cao H, Xia GJ, Chen JW, Yan HM, Huang Z, Wang YG. Mechanistic insight into oxygen reduction reaction on Mn1–N4/C single atom catalyst: the role of solvent environment. J Phys Chem C. 2020;124(13):7287.

[24] Zhong GY, Xu SR, Liu L, Zheng CZ, Dou JJ, Wang FY, Fu XB, Liao WB, Wang HJ. Effect of experimental operations on the limiting current density of oxygen reduction reaction evaluated by rotating-disk electrode. ChemElectroChem. 2020;7(5):1107.

[25] Shao MH, Chang QW, Dodelet JP, Chenitz R. Recent advances in electrocatalysts for oxygen reduction reaction. Chem Rev. 2016;116(6):3594.

[26] Shao YY, Dodelet JP, Wu G, Zelenay P. PGM-free cathode catalysts for PEM fuel cells: a mini-review on stability challenges. Adv Mater. 2019;31(31):1807615.

[27] Chung H, Cullen D, Higgins D, Sneed B, Holby E, More K, Zelenay P. Direct atomic-level insight into the active sites of a high-performance PGM-free ORR catalyst. Science. 2017;357(6350):479.

[28] Kattel S, Atanassovc P, Kiefer B. A density functional theory study of oxygen reduction reaction on non-PGM Fe–N_x–C electrocatalysts. Phys Chem Chem Phys. 2014;16(27):13800.

[29] Lai QX, Zheng LR, Liang YY, He J, Zhao J, Chen J. Metal–organic-framework-derived Fe–N/C electrocatalyst with five coordinated Fe–N_x sites for advanced oxygen reduction in acid media. ACS Catal. 2017;7(3):1655.

[30] Niu YL, Huang XQ, Hu WH. Fe_3C nanoparticle decorated Fe/N doped graphene for efficient oxygen reduction reaction electrocatalysis. J Power Sources. 2016;332:305.

[31] Li ZT, Sun HD, Wei LQ, Jiang WJ, Wu MB, Hu JS. Lamellar metal organic framework derived Fe–N–C non-noble electrocatalysts with bimodal porosity for efficient oxygen reduction. ACS Appl Mater Interfaces. 2017;9(6):5272.

[32] Zhou ZX, He F, Shen YF, Chen XH, Yang YR, Liu SQ, Mori T, Zhang YJ. Coupling multiphase-Fe and hierarchical N--doped graphitic carbon as trifunctional electrocatalysts by supramolecular preorganization of precursors. Chem Commun. 2017;53(12):2044.

[33] Song CS, Wu SK, Shen XP, Miao XL, Ji ZY, Yuan AH, Xu KQ, Liu MM, Xie XL, Kong LR, Zhu GX, Shah SA. Metal–organic framework derived Fe/Fe_3C@N-doped-carbon porous hierarchical polyhedrons as bifunctional electrocatalysts for hydrogen evolution and oxygen-reduction reactions. J Colloid Interface Sci. 2018;524(15):92.

[34] Shah SSA, Najam T, Cheng C, Peng LS, Xiang R, Zhang L, Deng JH, Ding W, Wei ZD. Exploring Fe–N_x for peroxide reduction: template-free synthesis of FeN_x traumatized mesoporous carbon nanotubes as an ORR catalyst in acidic and alkaline solutions. Chem Eur J. 2018;24(42):10630.

[35] Deng YJ, Chi B, Li J, Wang GH, Zheng L, Shi XD, Cui ZM, Du L, Liao SJ, Zang KT, Luo J, Hu YF, Sun XL. Atomic Fe-doped MOF-derived carbon polyhedrons with high active-center density and ultra-high performance toward PEM fuel cells. Adv Energy Mater. 2019;9(13):1802856.

[36] Chen XD, Wang N, Shen K, Xie YK, Tan YP, Li YW. MOF-derived isolated Fe atoms implanted in N-doped 3D hierarchical carbon as an efficient ORR electrocatalyst in both alkaline and acidic media. ACS Appl Mater Interfaces. 2019;11(29):25976.

[37] Jina HH, Zhou H, He DP, Wang ZH, Wu QL, Liang QR, Liu SL, Mu SC. MOF-derived 3D Fe–N–S co-doped carbon matrix/nanotube nanocomposites with advanced oxygen reduction activity and stability in both acidic and alkaline media. Appl Catal B. 2019;250(5):143.

[38] Guo DK, Han SC, Wang JC, Zhu YF. MIL-100-Fe derived N-doped Fe/Fe_3C@C electrocatalysts for efficient oxygen reduction reaction. Appl Surf Sci. 2018;434(15):1266.

[39] Gao SY, Fan BF, Feng R, Ye CL, Wei XJ, Xu J, Bu XH. N-doped-carbon-coated Fe_3O_4 from metal–organic framework as efficient electrocatalyst for ORR. Nano Energy. 2017;40: 462.

[40] Yang WX, Zhang YL, Liu SJ, Chen LL, Jia JB. In-situ forming Fe–N doped metal organic framework@carbon nanotubes/graphene hybrids for a rechargeable Zn–air battery. Chem Comm. 2017;53(96):12934.

[41] Yang WX, Zhang YL, Liu XJ, Chen LL, Liu MC, Jia JB. Polymerization-dissolution strategy to prepare Fe, N, S tri-doped carbon nanostructures for Zn–air batteries. Carbon. 2019;147:83.

[42] Huang XX, Yang ZY, Dong B, Wang YZ, Tang TY, Hou YL. In-situ Fe_2N@N-doped porous carbon hybrids as superior catalysts for oxygen reduction reaction. Nanoscale. 2017;9(24): 8102.

[43] Zheng L, Dong YY, Chi B, Cui ZM, Deng YJ, Shi XD, Du L, Liao SJ. UIO-66-NH_2-derived mesoporous carbon catalyst co-doped with Fe/N/S as highly efficient cathode catalyst for PEMFCs. Small. 2019;15(4):1803520.

[44] Tang C, Wang HF, Chen X, Li BQ, Hou TZ, Zhang BS, Zhang Q, Titirici MM, Wei F. Topological defects in metal-free nanocarbon for oxygen electrocatalysis. Adv Mater. 2016; 28(32):6845.

[45] Tan B, Luo H, Xie ZL. Formation of N-rich hierarchically porous carbon via direct growth ZIF-8 on C_3N_4 nanosheet with enhancing electrochemical performance. Chemistryselect. 2018;3(23):6440.

[46] Fu SF, Zhu CZ, Su D, Song JH, Yao SY, Feng S, Engelhard M, Du D, Lin YH. Porous carbon-hosted atomically dispersed iron–nitrogen moiety as enhanced electrocatalysts for oxygen reduction reaction in a wide range of pH. Small. 2018;14(12): 1703118.

[47] Yang Q, Xiao ZC, Kong DB, Zhang TL, Duan XG, Zhou SK, Niu Y, Shen YD, Sun HQ, Wang SB, Zhi LJ. New insight to the role of edges and heteroatoms in nanocarbons for oxygen reduction reaction. Nano Energy. 2019;66:104096.

[48] Zhong GH, Liu DX, Zhang JY. Applications of porous metal–organic framework MIL-100(M) (M = Cr, Fe, Sc, Al, V). Cryst Growth Des. 2018;18(12):7730.

[49] Seo YK, Yoon JW, Lee JS, Lee U, Hwang YK, Jun CH, Horcajada P, Serre C, Chang JS. Large scale fluorine-free synthesis of hierarchically porous iron(III) trimesate MIL-100(Fe) with a zeolite MTN topology. Microporous Mesoporous Mater. 2012;157(15):137.

[50] Skobelev I, Sorokin A, Kovalenko K, Fedin V, Kholdeeva O. Solvent-free allylic oxidation of alkenes with O_2 mediated by Fe- and Cr-MIL-101. J Catal. 2013;298:61.

[51] Han YJ, Zhai JF, Zhanga LL, Dong SJ. Direct carbonization of cobalt-doped NH_2-MIL-53(Fe) for electrocatalysis of oxygen evolution reaction. Nanoscale. 2016;8(2):1033.

[52] Guo DH, Shibuya R, Akiba C, Saji S, Kondo T, Nakamura J. Active sites of nitrogen-doped carbon materials for oxygen reduction reaction clarified using model catalysts. Science. 2016;351(6271):361.

[53] Cao L, Zhou XH, Li ZH, Su KM, Cheng BW. Nitrogen and fluorine hybridization state tuning in hierarchical honeycomb-like carbon nanofibers for optimized electrocatalytic ORR in alkaline and acidic electrolytes. J Power Sources. 2019;43(15):376.

[54] Peng HL, Liu FF, Liu XJ, Liao SJ, You CH, Tian XL, Nan HX, Luo F, Song HY, Fu ZY, Huang PY. Effect of transition metals on the structure and performance of the doped carbon catalysts derived from polyaniline and melamine for ORR application. ACS Catal. 2014;4(10):3797.

[55] Sanetuntikul J, Shanmugam S. High pressure pyrolyzed non-precious oxygen reduction catalysts for alkaline polymer electrolyte membrane fuel cells. Nanoscale. 2015;7(17):7644.

[56] Yan XC, Dong LD, Huang YC, Jia Y, Zhang LZ, Shen SH, Chen J, Yao XD. Probing the active sites of carbon-encapsulated cobalt nanoparticles for oxygen reduction. Small Methods. 2019;3(9):1800439.

[57] Zhao WP, Wan G, Peng CL, Sheng HP, Wen JG, Chen HG. Key single-atom electrocatalysis in metal–organic framework (MOF)-derived bifunctional catalysts. Chemsuschem. 2018; 11(19):3473.

[58] Cheng G, Liu GL, Liu P, Chen L, Han S, Han JX, Ye F, Song W, Lan B, Sun M, Yu L. Nitrogen-doped ketjenblack carbon supported Co_3O_4 nanoparticles as a synergistic electrocatalyst for oxygen reduction reaction. Front Chem. 2019;7:766.

[59] Qu HJ, Gao JJ, Wen YR, Shang B, Wang JQ, Lin X, Wang Y. Platinum cluster/nanoparticle on CoO nanosheets with coupled atomic structure and high electrocatalytic durability. ACS Appl Energy Mater. 2018;1(5):1840.

[60] Liu J, Bao HL, Zhang BS, Hua QF, Shang MF, Wang JQ, Jiang LH. Geometric occupancy and oxidation state requirements of cations in cobalt oxides for oxygen reduction reaction. ACS Appl Mater Interfaces. 2019;11(13):12525.

[61] Feng XH, Wu T, Carreon MA. Synthesis of ZIF-67 and ZIF-8 crystals using DMSO (dimethyl sulfoxide) as solvent and kinetic transformation studies. J Cryst Growth. 2016;455:152.

[62] Liu H, Wang MQ, Chen ZY, Chen H, Xu MW, Bao SJ. Design and synthesis of Co–N–C porous catalysis derived from metal organic complexes for high effective ORR. Dalton Trans. 2017;46(45):15646.

[63] Ma L, Wang R, Li YH, Liu XF, Zhang QQ, Dong XY, Zang SQ. Apically Co-nanoparticles-wrapped nitrogen doped carbon nanotubes from a single-source MOF for efficient oxygen reduction. J Mater Chem A. 2018;6(47):24071.

[64] Xu CY, Lin Z, Zhao D, Sun YL, Zhong YJ, Ning JQ, Zheng CC, Zhang ZY, Hu Y. Facile in situ fabrication of Co nanoparticles embedded in 3D N-enriched mesoporous carbon foam electrocatalyst with enhanced activity and stability toward oxygen reduction reaction. J Mater Sci. 2019;54(7): 5412.

[65] Guo HL, Feng QC, Zhu JX, Xu JS, Li QQ, Liu SL, Xu KW, Zhang C, Liu TX. Cobalt nanoparticle-embedded nitrogen-doped carbon/carbon nanotube frameworks derived from metal–organic framework for tri-functional ORR, OER and HER electrocatalysis. J Mater Chem A. 2019;7(8):3664.

[66] Ding DN, Shen K, Chen XD, Chen HR, Chen JY, Fan T, Wu RF, Li YW. Multi-level architecture optimization of MOF-templated Co-based nanoparticles embedded in hollow N-doped carbon polyhedra for efficient OER and ORR. ACS Catal. 2018;8(9):7879.

[67] Qi CL, Zhang L, Xu GC, Sun ZP, Zhao AH, Jia DZ. Co@Co_3O_4 nanoparticle embedded nitrogen-doped carbon architectures as efficient bicatalysts for oxygen reduction and evolution reactions. Appl Surf Sci. 2018;427:319.

[68] Zhang MD, Dai QB, Zheng HG, Chen MD, Dai LM. Novel MOF-derived Co@N–C bifunctional catalysts for highly efficient Zn–air batteries and water splitting. Adv Mater. 2018; 30(10):1705431.

[69] Li M, Bai L, Wu SJ, Wen XD, Guan JQ. Co/CoO_x nanoparticles embedded onto carbon for efficient catalysis of oxygen evolution and oxygen reduction reactions. Chemsuschem. 2018;11(10):1722.

[70] Li JJ, Xia W, Tang J, Tan HB, Wang JY, Kaneti YV, Bando Y, Wang T, He JP, Yamauchi Y. MOF nanoleaves as new

sacrificial templates for the fabrication of nanoporous Co–N$_x$/C electrocatalysts for oxygen reduction. Nanoscale Horiz. 2019; 4(4):1006.

[71] Wu ZF, Tan B, Ma W, Xiong WW, Xie ZL, Huang XY. Mg^{2+} incorporated Co-based MOF precursors for hierarchical CNT-containing porous carbons with ORR activity. Dalton Trans. 2018;47(8):2810.

[72] Liang ZZ, Zhang CC, Yuan HT, Zhang W, Zheng HQ, Cao R. PVP-assisted transformation of metal–organic framework into Co-embedded N-enriched meso/microporous carbon materials as bifunctional electrocatalysts. Chem Commun. 2018;54(54): 7519.

[73] Guan BY, Yu L, Lou XW. Formation of single-holed cobalt/N-doped carbon hollow particles with enhanced electrocatalytic activity toward oxygen reduction reaction in alkaline media. Adv Sci. 2017;4(10):1700247.

[74] Chen XD, Shen K, Chen JY, Huang BB, Ding DN, Zhang L, Li YW. Rational design of hollow N/Co-doped carbon spheres from bimetal-ZIFs for high-efficiency electrocatalysis. Chem Eng J. 2017;330(15):736.

[75] Cai SC, Wang R, Yourey W, Li JS, Zhang HN, Tang HL. An efficient bifunctional electrocatalyst derived from layer-by-layer self-assembly of a three-dimensional porous Co–N–C@graphene. Sci Bull. 2019;64(14):968.

[76] Guo J, Gadipelli S, Yang YC, Li ZG, Lu Y, Brett D, Guo ZX. An efficient carbon-based ORR catalyst from low temperature etching of ZIF-67 with ultra-small cobalt nanoparticles and high yield. J Mater Chem A. 2019;7(8):3544.

[77] Yi XR, He XB, Yin FX, Chen BH, Li GR, Yin HQ. Co–CoO–Co$_3$O$_4$/N-doped carbon derived from metal–organic framework: the addition of carbon black for boosting oxygen electrocatalysis and Zn–air battery. Electrochim Acta. 2019; 295:966.

[78] Park H, Oh S, Lee S, Choi S, Oh M. Cobalt- and nitrogen-codoped porous carbon catalyst made from core–shell type hybrid metal–organic framework (ZIF-L@ZIF-67) and its efficient oxygen reduction reaction (ORR) activity. Appl Catal B. 2019;246:322.

[79] Bhattacharyya S, Konkena B, Jayaramulu K, Maji TK. Synthesis of nano-porous carbon and nitrogen doped carbon dots from an anionic MOF: a trace cobalt metal residue in carbon dots promotes electrocatalytic ORR activity. J Mater Chem A. 2017;5(26):13573.

[80] Shah SSA, Peng LS, Najam T, Cheng C, Wu GP, Nie Y, Ding W, Qi XQ, Chen SG, Wei ZD. Monodispersed Co in mesoporous polyhedrons: fine-tuning of ZIF-8 structure with enhanced oxygen reduction activity. Electrochim Acta. 2017; 251:498.

[81] Li WX, Yu B, Wang XQ, Wang B, Zhang XJ, Yuang DX, Wang ZG, Chen YF. Encapsulating hollow (Co, Fe)P nanoframes into N, P-codoped graphene aerogel for highly efficient water splitting. J Power Sources. 2020;456:228015.

[82] Wang ZG, Liu JB, Hao X, Wang Y, Chen YF, Li PJ, Dong MD. Enhanced power density of a supercapacitor by introducing 3D-interfacial graphene. New J Chem. 2020;44(31): 13377.

[83] Zhang W, Jiang XF, Wang XB, Kaneti YV, Chen YX, Liu J, Jiang JS, Yamauchi Y, Hu M. Spontaneous weaving of graphitic carbon networks synthesized by pyrolysis of ZIF-67 crystals. Angew Chem Int Ed. 2017;56(29):8435.

[84] Wang R, Dong XY, Du J, Zhao JY, Zang SQ. MOF-derived bifunctional Cu$_3$P nanoparticles coated by a N, P-codoped carbon shell for hydrogen evolution and oxygen reduction. Adv Mater. 2017;30(6):1703711.

[85] Li JS, Zhou N, Song JY, Fu L, Yan J, Tang YG, Wang HY. Cu-MOF-derived Cu/Cu$_2$O nanoparticles and CuN$_x$C$_y$ species to boost oxygen reduction activity of ketjenblack carbon in Al–air battery. ACS Sustain Chem Eng. 2018;6(1):413.

[86] Xie YC, Zhang C, He XQ, Su JW, Parker White T, Griep M, Lin J. Copper-promoted nitrogen-doped carbon derived from zeolitic imidazole frameworks for oxygen reduction reaction. Appl Surf Sci. 2019;464:344.

[87] Lai Q, Zhu J, Zhao Y, Liang Y, He J, Chen J. Electrocatalysts: mOF-based metal-doping-induced synthesis of hierarchical porous Cu–N/C oxygen reduction electrocatalysts for Zn–air batteries. Small. 2017;13(30):1700740.

[88] Zhao J, Li C, Liu R. Designed echinops-like Ni@NiNC as efficient bifunctional oxygen electrocatalyst for zinc-air battery. ChemElectroChem. 2019;6(2):342.

[89] Yan W, Cao X, Wang R, Sha Y, Cui P, Cui S. S, N co-doped rod-like porous carbon derived from S, N organic ligand assembled Ni-MOF as an efficient electrocatalyst for oxygen reduction reaction. J Solid State Chem. 2019;275:167.

[90] Tyagi A, Kar KK, Yokoi H. Atomically dispersed Ni/Ni$_x$S$_y$ anchored on doped mesoporous networked carbon framework: boosting the ORR performance in alkaline and acidic media. J Colloid Interf Sci. 2020;571:285.

[91] Ji LQ, Yang J, Zhang ZY, Qian Y, Su Y, Han M, Liu HK. Enhanced catalytic performance for oxygen reduction reaction derived from nitrogen-rich tetrazolate-based heterometallic metal–organic frameworks. Cryst Growth Des. 2019;19(5):2991.

[92] Najam T, Cai X, Aslam MK, Tufail MK, Shah SSA. Nano-engineered directed growth of Mn$_3$O$_4$ quasinanocubes on N-doped polyhedrons: efficient electrocatalyst for oxygen reduction reaction. Int J Hydrog Energ. 2020;45(23):12903.

[93] Amiinu IS, Pu Z, Liu X, Owusu KA, Monestel HGR, Boakye FO, Zhang H, Mu S. Multifunctional Mo-N/C@MoS$_2$ electrocatalysts for HER, OER, ORR, and Zn–air batteries. Adv Funct Mater. 2017;27(44):1702300.

[94] Li JJ, Xia W, Wang T, Zheng LR, Lai Y, Pan JJ, Jiang C, Song L, Wang MY, Zhang HT, Chen N, He JP. A facile way to construct effective Cu–N$_x$ active sites for oxygen reduction reaction. Chem Eur J. 2020;26(18):4070.

[95] Li F, Han G, Noh H, Kim S, Lu Y, Jeong H, Fu Z, Baek J. Boosting oxygen reduction catalysis with abundant copper single atom active sites. Energy Environ Sci. 2018;11:2263.

[96] Zhao X, Liu X, Huang B, Wang P, Pei Y. Hydroxyl group modification improves the electrocatalytic ORR and OER activity of graphene supported single and bi-metal atomic catalysts (Ni Co, and Fe). J Mater Chem A. 2019;7(42):24583.

[97] Gao QQ. A DFT study of the ORR on M–N3 (M = Mn, Fe Co, Ni, or Cu) co-doped graphene with moiety-patched defects. Ionics. 2020;26(5):2453.

[98] Kattel S, Wang G. A density functional theory study of oxygen reduction reaction on Me–N4 (Me = Fe Co, or Ni) clusters between graphitic pores. J Mater Chem A. 2013;1(36):10790.

[99] Wang MQ, Ye C, Wang M, Li TH, Yu YN, Bao SJ. Synthesis of M (Fe$_3$C Co, Ni)-porous carbon frameworks as high-efficient ORR catalysts. Energy Storage Mater. 2018;11:112.

[100] Jin K, Chu A, Park J, Jeong D, Jerng S, Sim U, Jeong H, Lee C, Park Y, Yang K, Pradhan G, Kim D, Sung N, Kim S, Nam K. Partially oxidized sub-10 nm MnO nanocrystals with high activity for water oxidation catalysis. Sci Rep. 2015;5(1): 10279.

[101] Zhang B, Cheng G, Lan B, Zheng X, Sun M, Ye Y, Yu L, Cheng X. Crystallization design of MnO$_2$ via acid towards better oxygen reduction activity. Cryst Eng Comm. 2016; 18(36):6895.

[102] Li T, Xue B, Wang B, Guo G, Han D, Yan Y, Dong A. Tubular monolayer superlattices of hollow Mn$_3$O$_4$ nanocrystals and their oxygen reduction activity. J Am Chem Soc. 2017; 139(35):12133.

[103] Tang Q, Jiang L, Liu J, Wang S, Sun G. Effect of surface manganese valence of manganese oxides on the activity of the oxygen reduction reaction in alkaline media. ACS Catal. 2014; 4(2):457.

[104] Zhu D, Liu J, Zhao Y, Zheng Y, Qiao SZ. Engineering 2D metal–organic framework/MoS_2 interface for enhanced alkaline hydrogen evolution. Small. 2019;15(14):1805511.

[105] Xu X, Xu H, Cheng D. Design of high-performance MoS_2 edge supported single-metal atom bifunctional catalysts for overall water splitting via a simple equation. Nanoscale. 2019;11(42): 20228.

[106] Hao Y, Gong P, Xu LC, Pu J, Wang L, Huang LF. Contrasting oxygen reduction reactions on zero- and one dimensional defects of MoS_2 for versatile applications. ACS Appl Mater Interfaces. 2019;11(49):46327.

[107] Wang ZG, Li Q, Xu HX, Dahl-Petersen C, Yang Q, Cheng DJ, Cao DP, Besenbacher F, Lauritsen J, Helveg S, Dong MD. Controllable etching of MoS_2 basal planes for enhanced hydrogen evolution through the formation of active edge sites. Nano Energy. 2018;49:634.

[108] Xia H, Zhang J, Yang Z, Guo S, Guo S, Xu Q. 2D MOF nanoflake-assembled spherical microstructures for enhanced supercapacitor and electrocatalysis performances. Nano-Micro Lett. 2017;9(4):43.

[109] Wu M, Hu X, Li C, Li J, Zhou H, Zhang X, Liu R. Encapsulation of metal precursor within ZIFs for bimetallic N-doped carbon electrocatalyst with enhanced oxygen reduction. Int J Hydrog Energy. 2018;43(31):14701.

[110] Wang N, Li Y, Guo Z, Li H, Hayase S, Ma T. Synthesis of Fe, Co incorporated in P-doped porous carbon using a metal–organic framework (MOF) precursor as stable catalysts for oxygen reduction reaction. J Electrochem Soc. 2018;165(12): G3080.

[111] Dong Z, Liu G, Zhou S, Zhang Y, Zhang W, Fan A, Zhang X, Dai X. Restructured Fe–Mn alloys encapsulated by N-doped carbon nanotubes catalysts derived from bimetallic MOF for enhanced oxygen reduction reaction. ChemCatChem. 2018; 10(23):5475.

[112] Xia W, Li J, Wang T, Song L, Guo H, Gong H, Jiang C, Gao B, He J. A synergistic effect of Ceria and Co in N-doped leaf-like carbon nanosheets derived from two-dimensional metal–organic framework and their enhanced performance in oxygen reduction reaction. Chem Commun. 2018;54(31):1623.

[113] Li ZH, He HY, Cao HB, Sun SM, Diao WL, Gao DL, Lu PL, Zhang SS, Guo Z, Li MJ, Liu RJ, Ren DH, Liu CM, Zhang Y, Yang Z, Jiang JK, Zhang GJ. Atomic Co/Ni dual sites and Co/Ni alloy nanoparticles in N-doped porous Janus-like carbon frameworks for bifunctional oxygen electrocatalysis. Appl Catal B. 2019;240:112.

[114] Xu Y, Huang Z, Wang B, Liang Z, Zhang C, Wang Y, Zhang W, Zheng H, Cao R. A two-dimensional multi-shelled metal–organic framework and its derived bimetallic N-doped porous carbon for electrocatalytic oxygen reduction. Chem Commun. 2019;55(98):14805.

[115] Wang ZG, Wu HH, Li Q, Besenbacher F, Li YR, Zeng XC, Dong MD. Reversing interfacial catalysis of ambipolar WSe_2 single crystal. Adv Sci. 2019;7(3):1901382.

Hua-Li Long is an associate professor of Hubei university. She received her Bachelor's degree and Ph.D. degree from Sichuan University. Her main research interests are the synthesis and characterization of catalytic materials and their applications in energy conversion and environmental protection.

Ming Li is a full professor of Hubei university. He received his Bachelor's degree from Huazhong University of Science and Technology, Master's degree from Tsinghua University and Ph.D. degree from ETH Zurich, Switzerland. His main research interests are the synthesis of 2D polymeric materials and framework materials and their applications in electronics, energy conversion, environmental protection and so on.